Title

Evolution of fluid–rock interaction in the Reykjanes geothermal system, Iceland: Evidence from Iceland Deep Drilling Project core RN-17B

Permalink

https://escholarship.org/uc/item/0hh223p1

Authors

Fowler, Andrew PG
Zierenberg, Robert A
Schiffman, Peter
et al.

Publication Date

2015-09-01

DOI

10.1016/j.jvolgeores.2015.06.009

Peer reviewed

Evolution of fluid–rock interaction in the Reykjanes geothermal system, Iceland: Evidence from Iceland Deep Drilling Project core RN-17B

CrossMark

Andrew P.G. Fowler [a,*], Robert A. Zierenberg [a], Peter Schiffman [a], Naomi Marks [b], Guðmundur Ómar Friðleifsson [c]

[a] Department of Earth and Planetary Sciences, University of California, Davis, CA 95616, USA
[b] Lawrence Livermore National Laboratory, 7000 East Avenue, Livermore, CA 94550, USA
[c] HS Orka, hf, Reykjanesbaer, Iceland

ARTICLE INFO

ABSTRACT

We describe the lithology and present spatially resolved geochemical analyses of samples from the hydrothermally altered Iceland Deep Drilling Project (IDDP) drill core RN-17B. The 9.3 m long RN-17B core was collected from the seawater-dominated Reykjanes geothermal system, located on the Reykjanes Peninsula, Iceland. The nature of fluids and the location of the Reykjanes geothermal system make it a useful analog for seafloor hydrothermal processes, although there are important differences. The recovery of drill core from the Reykjanes geothermal system, as opposed to drill cuttings, has provided the opportunity to investigate evolving geothermal conditions by utilizing in-situ geochemical techniques in the context of observed paragenetic and spatial relationships of alteration minerals. The RN-17B core was returned from a vertical depth of ~2560 m and an in-situ temperature of ~345 °C. The primary lithologies are basaltic in composition and include hyaloclastite breccia, fine-grained volcanic sandstone, lithic breccia, and crystalline basalt. Primary igneous phases have been entirely pseudomorphed by calcic plagioclase + magnesium hornblende + chlorite + titanite + albitized plagioclase + vein epidote and sulfides. Despite the extensive hydrothermal metasomatism, original textures including hyaloclastite glass shards, lithic clasts, chilled margins, and shell-fragment molds are superbly preserved. Multi-collector LA-ICP-MS strontium isotope ratio ($^{87}Sr/^{86}Sr$) measurements of vein epidote from the core are consistent with seawater as the dominant recharge fluid. Epidote-hosted fluid inclusion homogenization temperature and freezing point depression measurements suggest that the RN-17B core records cooling through the two-phase boundary for seawater over time to current in-situ measured temperatures. Electron microprobe analyses of hydrothermal hornblende and hydrothermal plagioclase confirm that while alteration is of amphibolite-grade, it is in disequilibrium and the extent of alteration is dependent upon protolith type and water/rock ratio. Alteration in the RN-17B core bares many similarities to that of Type II basalts observed in Mid-Atlantic Ridge samples.

1. Introduction

Due to the technical challenges and great expense of seafloor drilling, only four drill holes that exceed 1000 m into oceanic basement rock have been completed (Ildefonse et al., 2007). The location of the Reykjanes geothermal system on the immediate subaerial extension of the Mid-Atlantic Ridge coupled with seawater recharge fluids makes it a useful analog for seafloor hydrothermal alteration (Spooner and Fyfe, 1973; Spooner, 1974). In contrast to seafloor systems, drill cutting samples are available to depths exceeding 3000 m from the Reykjanes geothermal system thanks to the 38 geothermal wells associated with a 100-megawatt geothermal power plant.

Important differences between Reykjanes and seafloor systems include evidence for a period of meteoric fluid recharge during the Pleistocene, when a substantial icesheet was present (Sveinbjörnsdóttir et al., 1986; Franzson et al., 2002; Pope et al., 2009; Marks et al., 2010). The Reykjanes geothermal system also lacks the hydrostatic pressure of overlying cold seawater; therefore much greater depths must be reached before the venting temperatures observed in seafloor hydrothermal systems are achieved. Another proposed difference is that lithologies at depth in the Reykjanes geothermal system were deposited in a shallow marine setting and are at the current depth due to high rates of subsidence (Friðleifsson and Richter, 2010). With the exception of Friðleifsson and Richter (2010), previous studies relied on drill cutting samples.

Drill core has only recently been recovered from three locations in the Reykjanes geothermal system: a relatively unaltered ~2 m long core from RN-19 recovered at an in-situ temperature between 250

and 260 °C (Friðleifsson and Richter, 2010), the 9.3 m RN-17B core that is the subject of this study, recovered at an in situ temperature of 345 °C (Friðleifsson and Richter, 2010; Friðleifsson et al., 2011), and three sequential cores totaling 22.5 m from RN-30 (estimated temperature based on depth to the boiling curve approximately 365 °C, although an in-situ temperature measured after the hole has thermally equilibrated following drilling was not available at the time of this writing). These 4 inch diameter cores permit the study of basalt–seawater interaction at high in-situ temperatures.

Drill core preserves the textural relationships between hydrothermal minerals, which can be recognized by sequential deposition in voids and fractures, replacement textures, compositional zoning of mineral grains, and cross-cutting veins. Conversely, drill cuttings from the same depth intervals are ≪1/4 in. in diameter (thus preserving limited spatial mineralogical relationships), represent depth intervals that are potentially intermixed during ascent of the drilling fluid, and are returned from uncertain depth intervals because recovery time lags behind the actual drill depth. Drill core provides an accurate in situ depth record and provides the opportunity to evaluate spatial relationships of alteration mineralogy to a degree not possible from drill cuttings. The recovery of drill core from deeper portions of the Reykjanes geothermal system provides an important opportunity to make comparisons with drill core recovered from submarine hydrothermal systems collected by the Ocean Drilling Program (ODP).

The focus of this study is the hydrothermally altered RN-17B core. Well RN-17 (Fig. 1) was drilled in the Reykjanes geothermal system to a depth of 2266 m when the drill rod broke, requiring a sidetrack hole to reach the targeted depth of 2700 m (Friðleifsson et al., 2005). RN-17 was completed as a vertical well with a total depth of 3082.4 m in February 2005. RN-17 subsequently suffered a formation collapse during a flow test. The well was re-entered in 2009 and sidetrack hole RN-17B was directionally drilled (SSW; 35° from vertical) from a kick off point at approximately 920 m depth, and eventually reached a down hole depth of 3077 m (Friðleifsson et al., 2005; Helgadóttir et al., 2009; Friðleifsson and Richter, 2010). Drill cuttings were collected during the drilling of RN-17 and RN-17B at 2 m intervals, and larger samples of cuttings intended for geochemical analysis were collected at 50 m intervals. In addition, a 4-inch diameter drill core was taken from a down-hole depth of 2798.5 m to 2807.8 m (ca. 2560 to 2570 m vertical depth) in RN-17B, at an in-situ temperature of 345 °C (Friðleifsson and Richter, 2010; Friðleifsson et al., 2011).

We provide details of the lithology and variable geothermal conditions in the Reykjanes geothermal system at a resolution not previously possible using drill cutting samples. We suggest that the lithologies present in the RN-17B core resemble hyaloclastite deposits formed during submarine volcanic and subsequent epiclastic processes described for deep marine portions of the Reykjanes Ridge. Fluid inclusion measurements from epidote veins in the RN-17B core record temperatures cooling through the two-phase boundary for seawater to current temperatures. Cooling of the geothermal system was coupled with a decrease in water/rock ratio. Epidote veins in the RN-17B core do not record an early period of meteoric alteration. The results of this study provide insight into evolving hydrothermal process in a setting analogous to shallow submarine hydrothermal systems.

We support the conclusions of this study using: (1) a detailed lithological log of the RN-17B core; (2) electron microprobe analyses of vein epidote, hydrothermal hornblende, and altered relict igneous plagioclase; (3) homogenization temperature and freezing point depression measurements of fluid inclusions hosted in epidote veins; and (4) strontium isotope ratio (^{87}Sr/^{86}Sr) measurements of vein epidote using laser ablation multi collector ICP-MS (LA-ICP-MS). We present and discuss our results in the context of seafloor hydrothermal systems, and highlight key similarities and differences.
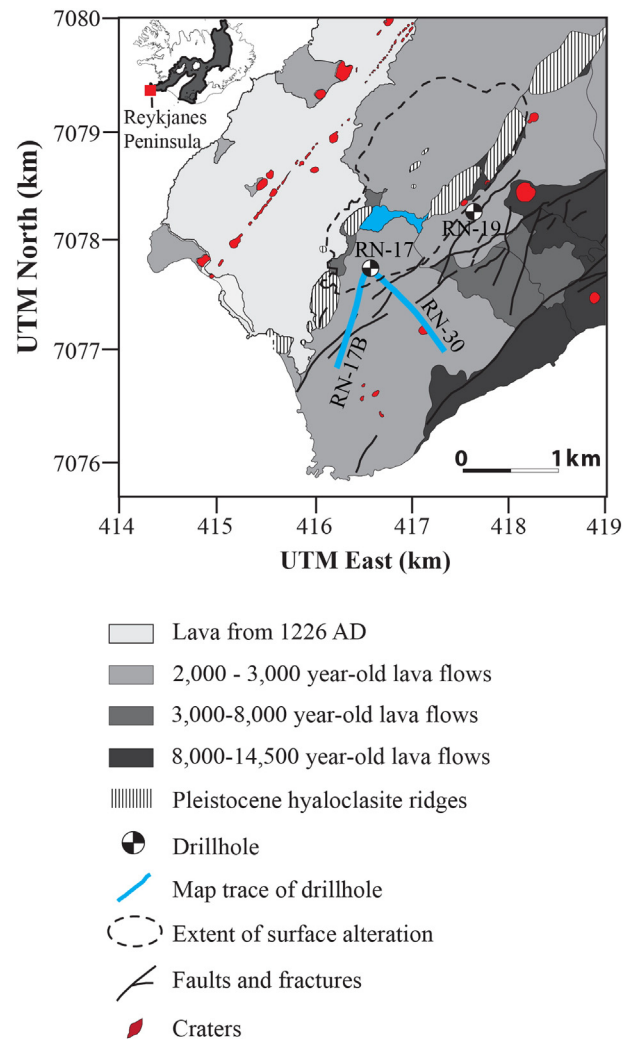

Fig. 1. Location of the Reykjanes geothermal system, Iceland. Wells discussed in the text are indicated.
Modified after Marks et al. (2010) and Sæmundsson, K. (2011).

2. Geological setting

The Reykjanes volcanic system is the subaerial continuation of the submarine Reykjanes ridge. The volcanic system is hosted in an oblique extensional tectonic setting, resulting in episodic fissure eruptions (Clifton and Kattenhorn, 2006). Tectonic extension-controlled structures and active volcanism have resulted in significant geothermal activity along the Reykjanes Peninsula, notably in the Reykjanes and Svartsengi geothermal systems (Jakobsson et al., 1978; Arnórsson, 1995). The Reykjanes geothermal system is located on the western tip of the Reykjanes Peninsula, approximately 50 km southwest of Reykjavík (Fig. 1).

The Reykjanes geothermal fluid is seawater, chemically modified due to boiling and fluid/rock interaction (Tómasson and Kristmannsdóttir, 1972; Arnórsson, 1978; Ólafsson and Riley, 1978; Arnórsson, 1995; Bird and Spieler, 2004; Friðleifsson and Elders, 2005; Marks et al., 2010). Compared to seawater, hydrothermal fluids in the Reykjanes geothermal system have similar concentrations of Na and Cl; increased concentrations of K, Ca, SiO$_2$, Fe, and Al; and decreased concentrations of SO$_4$ and Mg indicating that mineral precipitation, and significant water rock interaction have occurred (Lonker et al., 1993; Arnórsson, 1995; Pope et al., 2009).

Alteration zones based on the appearance of index minerals have been established for the Reykjanes geothermal system (i.e., Tómasson

and Kristmannsdóttir, 1972; Kristmannsdóttir, 1975; Lonker et al., 1993; Franzson et al., 2002; Friðleifsson et al., 2005; Marks et al., 2010, 2011). The progressive alteration zones determined from RN-17 drill cuttings are: smectite–zeolite (0–312 m), epidote–mixed layer clay (MLC) (312–520 m), chlorite–epidote (520–1200 m), epidote–actinolite (1200–2350 m), and amphibole (2350–3082 m). Sidetrack hole RN-17B shows a similar progression in alteration with depth. Localized high-grade granoblastic hornblende hornfels and pyroxene hornfels zones resulting from contact metamorphism were identified in drill cuttings at depths of 2150 m and intervals in the depth range 2600–2850 m from RN-17 (Marks et al., 2011).

Epidote–MLC, chlorite–epidote, and epidote–actinolite alteration zones in RN-17 and RN-17B fall within the greenschist metamorphic facies, while the amphibole alteration zone, defined by the presence of hornblendic amphibole and calcic plagioclase, falls within the amphibolite metamorphic facies (Marks et al., 2011). The transition from greenschist assemblages to amphibolite assemblages coincides with a change in amphibole composition from actinolite to hornblende accompanied with the presence of calcic plagioclase, while epidote and chlorite remain stable (Marks et al., 2011). The RN-17B core falls into the amphibole alteration zone. The alteration to calcic plagioclase + magnesium hornblende + chlorite + titanite + albitized plagioclase + vein epidote and sulfides is similar to that of Type II basalts observed in Mid-Atlantic Ridge samples, where it is proposed that a reaction zone is present where the composition of hydrothermal fluids actively venting on the seafloor acquire their geochemical characteristics (Gillis and Thompson, 1993).

The shallow depth at which greenschist-equivalent alteration assemblages are encountered, relative to the present day temperature–depth relation controlled by a boiling hydrostatic curve, indicates that the Reykjanes geothermal system experienced hotter temperatures and higher pressures in the past (Sveinbjörnsdóttir et al., 1986; Franzson et al., 2002; Friðleifsson et al., 2005; Marks et al., 2010). The salinity of fluid inclusions in quartz, plagioclase, and calcite in wells RN-9 and RN-10 (Franzson et al., 2002), along with deuterium and oxygen isotope studies of fluids and alteration minerals, have been used to suggest an evolution of hydrothermal fluids from meteoric to seawater (Ólafsson and Riley, 1978; Sveinbjörnsdóttir et al., 1986; Lonker et al., 1993; Pope et al., 2009; Marks, 2010). The postulated evolving temperature conditions and fluid compositions in the Reykjanes geothermal system have been attributed to the presence of a substantial ice sheet overlying the Reykjanes Peninsula during the Pleistocene, providing a mechanism for fresh water recharge and increased pressure, which raised the boiling point curve and resulted in the formation of anomalously shallow, high-temperature alteration minerals (Sveinbjörnsdóttir et al., 1986; Friðleifsson et al., 2005).

3. Methods

3.1. Fluid inclusions

Fluid inclusion melting point (T_m) and homogenization temperature (T_h) measurements were performed on fluid inclusions hosted by epidote crystals in veins at depths of 2798.15 and 2800.05 m in the RN-17B core. Salinity, as weight sodium chloride (wt.% NaCl), was calculated from freezing point depression (FPD) measurements using the equation of Bodnar (1993).

Fluid inclusion samples were prepared from doubly polished thin sections cut to a thickness of 100 μm and mounted on glass slides at room temperature with acetone-soluble epoxy. Fluid inclusions were identified and mapped on the prepared sections prior to floating the samples from the glass slides by dissolving the epoxy with acetone. T_h and T_m were measured using a Fluid Inc. adapted USGS gas-flow heating/freezing system equipped with a petrographic microscope, calibrated using synthetic H_2O fluid inclusions trapped at the critical point of water and synthetic CO_2 fluid inclusions. Homogenization of

fluid inclusions was verified by cycling the temperature to ensure that the vapor bubble did not readily nucleate. Care was taken to keep measured fluid inclusions within 1 mm of the thermocouple tip to minimize irreproducibility due to thermal gradient effects. Repeated measurements of the standards reproduced the known T_h by ± 0.2 °C (which equates to ± 0.4 wt.% NaCl), and T_h by ± 0.3 °C, a similar range to that reported by Kelley and Delaney (1987). The precision of our T_m measurements is consistent with that reported in previous studies (Kelley and Delaney, 1987; Vanko, 1988). Results in Fig. 5 are presented using a more conservative estimate for T_h error of ± 5 °C, which accounts for ± 2 °C thermal gradient effects due to sample distance from the thermocouple, ± 1 °C for thermocouple accuracy, and ± 2 °C for bracketing of the homogenization temperature (Vanko, 1988). Upon completion of T_m and T_h measurements, fluid inclusion chips were mounted on 1-inch diameter Plexiglas™ rounds with double-sided sticky tape for major element and strontium isotope analyses.

3.2. Major element mineral chemistry

Mineral identification and major element analyses were performed at UC Davis using a Cameca SX-100 electron microprobe (EMP). Mineral identification was completed qualitatively on carbon-coated thin sections using the energy-dispersive spectrometry (EDS) capabilities of the EMP. Quantitative EMP analyses were performed on epidote crystals hosting fluid inclusions, vein epidote, and zoned epidote crystals. EMP analyses were performed on amphibole in altered hyaloclastite shards, the altered quenched margin of a crystalline clast, amygdales, vein selvages, and altered crystalline clasts. EMP analyses were also performed on relict igneous plagioclase phenocrysts in altered crystalline clasts.

Epidote analyses were performed using an accelerating voltage of 15 kV, a beam current of 15 nA (100 nA for Sr), a nominal beam diameter of 1 μm, and a peak counting time of 10 s (60 s for Sr). The calibration standards included Ti (Taylor rutile), Fe (Taylor hematite), Ca, Al, and Si (Smithsonian anorthite), Mg (tremolite from Campolungo, Switzerland), Mn (rhodonite; Harvard collection #104791), and Sr ($SrAl_2Si_2$ synthesized by Naohito Tsujii). The mole fraction of Fe (X_{Fe}) was calculated using the equation $X_{Fe} = Fe^{3+} / (Fe^{3+} + Al^{3+})$. The nomenclature X_{Fe} in lieu of pistacite component (X_{Ps}) is used in this study, after Armbruster et al. (2006).

Amphibole analyses were performed using an accelerating voltage of 15 kV, beam current of 10 nA, a nominal beam diameter of 5 μm, and a peak counting time of 10 s. The calibration standards included Ti (Taylor rutile), Ca (Taylor wollastonite), Fe (Taylor hematite), Al (Smithsonian anorthite), Mg and Si (tremolite from Campolungo, Switzerland), Na (jadeite from Clear Creek, California), Mn (rhodonite; Harvard collection #104791), and K (orthoclase).

Plagioclase analyses were performed using an accelerating voltage of 15 kV, beam current of 10 nA, a nominal beam diameter of 5 μm, and a peak counting time of 10 s. The calibration standards included Na and Si (Taylor albite), Ca (Taylor wollastonite), Fe (Taylor hematite), Al (Smithsonian anorthite), and K (orthoclase).

3.3. Strontium isotope chemistry

^{88}Sr, ^{87}Sr, ^{86}Sr, ^{85}Rb, and ^{84}Sr were measured simultaneously in epidote crystals hosting measured fluid inclusions, and in transects across a vein from 2800.05 m using laser ablation multi-collector inductively coupled plasma mass spectrometry (LA-MC-ICP-MS). Analyses were performed at UC Davis using a Thermo Scientific Neptune multicollector coupled to a Photon Instruments laser ablation system equipped with a 193 nm excimer laser and a dual volume sample cell. Helium was used as the aerosol carrier gas and mixed with argon prior to introducing ablated aerosol into the plasma torch. A flow rate of 1.3 l/min was obtained for argon, the outer containment of the dual cell had a helium flow rate of 0.75 l/min, and the inner cup had a helium

flow rate of 0.13 l/min. Laser conditions consisted of a laser spot size of 60 μm, 8 Hz repetition rate and 1.8 J/cm² fluence.

An internal deep-sea coral standard (DWC; modern coral with homogenous $^{87}Sr/^{86}Sr$ composition verified previously by standardization to marine fish otoliths) was used to calibrate the $^{87}Sr/^{86}Sr$ ratio of seawater. The $^{87}Sr/^{86}Sr$ ratio of fresh volcanic rock (not exposed to seawater) was calibrated using plagioclase phenocrysts in rhyolite magma quenched to glass, obtained from the IDDP-01 well in the meteoric water-dominated Krafla geothermal field, Iceland (Zierenberg et al., 2013). Plagioclase in the Krafla sample was chosen as a standard to replicate as closely as possible the silicate laser ablation characteristics expected from epidote. Standards were analyzed at the start of the sample run and after every 10 samples.

Background concentrations were measured for a period of 1 min prior to sample ablation. Samples were ablated for a minimum of 200 cycles. Individual sample counts were excluded from the analysis if they fell outside of a 2 standard error range. The background signal and ^{87}Rb interference were automatically subtracted and corrected for by Neptune software.

4. Results

4.1. Lithology

Preliminary lithological observations for the RN-17B core are described in Friðleifsson and Richter (2010), Marks (2010) and Marks et al. (2010). A detailed core log is included as an electronic appendix. Four distinct lithologies are present in the core: pillow basalt breccia, hyaloclastite breccia, lithic breccia, and volcanic sandstone. Two types of basalt are also present in the core: plagioclase–phyric basalt with 2–3 mm long altered igneous plagioclase phenocrysts; and olivine–phyric basalt with microcrystalline (<0.05 mm long) plagioclase laths and sparse 0.5–1 mm chloritized olivine phenocrysts. For ease of description, the core has been divided into five units. The stratigraphic top of each unit is defined by the presence of poorly laminated volcanic sandstone that exhibits characteristics of transport from the sediment source area (Fig. 2).

Unit 1 is a clast-supported homolithic hyaloclastite breccia composed of vesicular and non-vesicular 20 to 80 mm plagioclase–phyric basalt clasts. Clasts are predominantly composed of felted or feathery green hornblende with fine titanite, and dusty, albitized igneous plagioclase laths. Vesicles in clasts are 1 to 4 mm in diameter, rimmed by green acicular hornblende and dominantly filled with dusty white albite and minor anhedral epidote. Basalt clast partly surrounded by quenched margins and are in a matrix of abundant 0.1 to 1.5 mm blocky hyaloclastite glass shards altered to coarse, felted to radial brown hornblende with fine titanite. Some sand-sized grains of crystalline basalt are also present in the hyaloclastite, identifiable by the presence of large, altered igneous plagioclase laths. The hyaloclastite matrix is sealed with dusty white albite and sparse, anhedral epidote and acicular green hornblende. This unit is interpreted as a pillow basalt breccia with limited down-slope transport from the site of eruption. Representative textures described in the text are indicated in Fig. 3.

Unit 2 is a clast-supported homolithic hyaloclastite breccia with plagioclase–phyric basalt clasts ranging in size from 3 mm to greater than the core diameter. A plagioclase–phyric basalt pillow is present within the hyaloclastite breccia at ~2800.4 m. Alteration in the quenched margins of plagioclase–phyric basalt clasts consists of coarse felted green hornblende + titanite. Calcic plagioclase occurs in <1 mm veins in the basalt pillow. Alteration in the crystalline centers of plagioclase–phyric clasts consists of green hornblende in a chloritic matrix intergrown with sparse, microcrystalline calcic plagioclase. Vesicles, which are uncommon, measure 0.1 to 0.2 mm diameter and are filled with fine white acicular actinolite and epidote: some retain open space. Basalt clast margins are chilled against a matrix of abundant blocky 0.1 to 1.5 mm hyaloclastite glass shards. Shard edges are altered
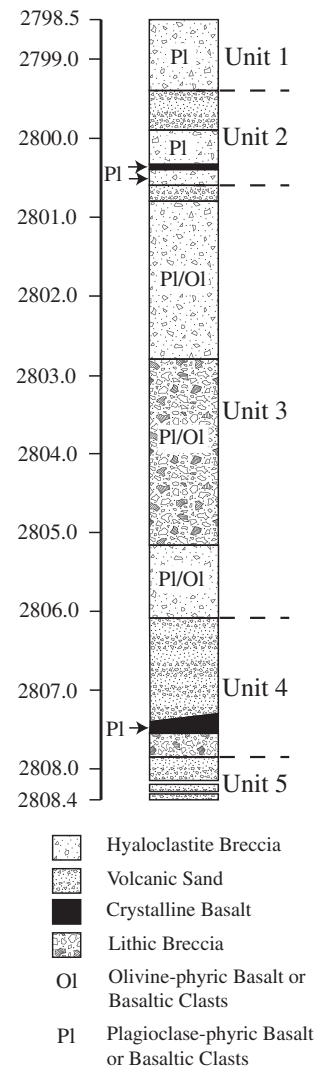

Fig. 2. Simplified RN-17B core log. A detailed core log is included as an electronic resource.

to coarse, felted to radial brown hornblende + titanite with sub-spherical epidote centers. Rare, uralitized pyroxene grains are distributed throughout the hyaloclastite matrix. Unit 2 is capped by lithic volcanic sandstone with crudely defined graded laminations. The sandstone is composed of glass shards and crystalline grains ranging in size from 0.3 to 1 mm and rare fragmented vesicular basalt clasts up to 20 mm wide with chilled margins on one side. This section of hyaloclastite, pillow breccia, and the apparently intact pillow lobe may have erupted in-situ.

Unit 3 is a matrix supported heterolithic breccia with hyaloclastite matrix grading down into a matrix of sand-sized crystalline basalt grains at 2802.8 m, and back into hyaloclastite matrix at 2805.2 m. Breccia clasts are sand-sized to 40 mm and are composed of both plagioclase–phyric and olivine–phyric basalt. Clasts appear fragmented, generally with chilled margins on one side only. The matrix is composed of detrital albitized plagioclase, chloritized olivine, hyaloclastite shards, and rounded sand-sized grains of basaltic composition. Alteration in clasts, matrix, and amygdales is similar to that in Units 1 and 2.

Unit 4 consists of crudely bedded volcanic sandstone overlaying a vesicular, plagioclase–phyric basalt pillow at 2807.5 m. The volcanic sandstone contains bivalve shell fragments that have been replaced by epidote (Friðleifsson and Richter, 2010). The crudely laminated volcanic sandstone is in contact with the pillow at an angle 55° to the core axis. Alteration in the center of the pillow consists of albitized relict igneous plagioclase laths, feathery green hornblende + fine titanite, abundant
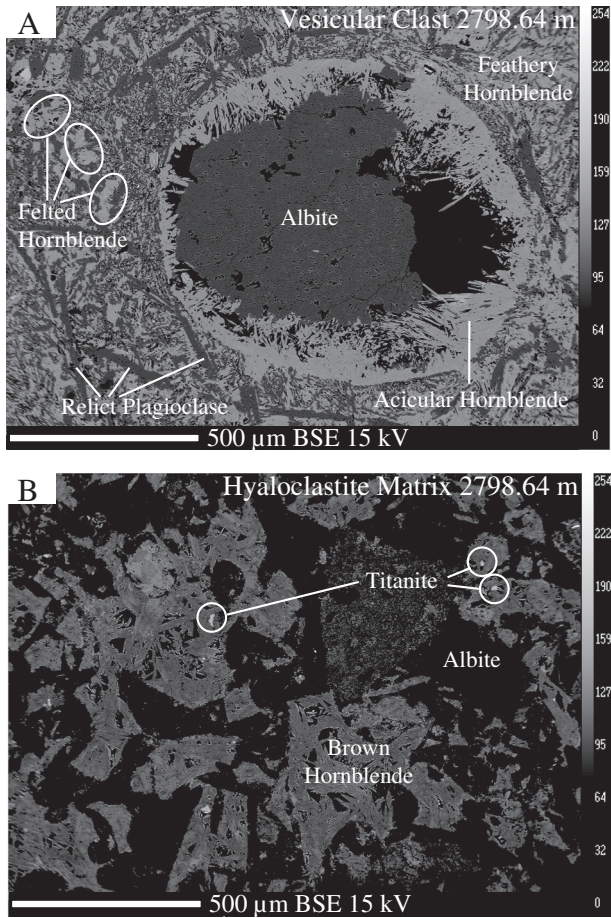
Fig. 3. BSE images indicating some typical textures described in the text for the RN-17B core. Panel A is a clast within an altered hyaloclastite matrix (B).

pyrite intergrown with magnetite, and rare patches of chlorite. Alteration on the edge of the pillow consists of coarse, felted green hornblende + fine titanite, and altered relict igneous plagioclase laths. Vesicles are similar to those in Unit 1. Below the pillow, at the base of the unit, is a volcanic breccia composed of plagioclase–phyric basalt clasts. Poorly defined bedding in the volcanic sandstone, the depositional contact of the hyaloclastite on the underlying pillow basalt, and a geopetal fill in a void interpreted to be a replaced bivalve shell, all dip at an angle of ~55° to the core axis, which suggests that these features have not been significantly tilted from horizontal given that the drill hole is inclined at 35°.

Unit 5 is fine-grained volcanic sandstone with occasional hyaloclastite shards. Unit 5 has crude laminations oriented 55° to the core axis at the top, grading down into coarser grained sedimentary breccia with no laminations and clasts up to 5 mm. Amygdales in clasts are filled with epidote. Sedimentary voids and matrix are filled with albite, acicular green hornblende and epidote. The base of the unit consists of large clasts with chilled margins.

The core is riddled with epidote-mineralized veins and fractures <1 to 20 mm wide, which are inclined ~30° or ~50° relative to the core axis. Although the core is not oriented, these vein orientations likely correspond approximately to vertical and horizontal veins, respectively. Thicker veins are more abundant in Units 1 and 2 and have an outer generation of clear epidote + pyrite and an inner generation of yellow epidote, as observed in thin section. Green acicular hornblende + epidote ± chlorite ± albite occur in vein selvages. Fracture surfaces in Unit 2 are coated with fibrous white actinolite (identified by refractive index) + pyrite + chalcopyrite + rare sphalerite. Discontinuous veins

of epidote + minor albite up to 6 mm wide with chlorite selvages are cut by steeper 1 mm wide epidote + pyrite veins with chlorite selvages that are oriented ~60° to the core axis.

4.2. Fluid inclusions

Fluid inclusions were identified in epidote samples from 2799.15 m and 2800.05 m. Fluid inclusions present parallel to cleavage along the {001} crystallographic axis were elongate and frequently tapered, some were planar in shape (Fig. 4A). Fluid inclusions concentrated in concentric growth rings perpendicular to the {001} crystallographic axis were generally equant and planar, some were tapered (Fig. 4B and C). Concentric growth zoning was identified in transmitted light based on fluid inclusion densities and slight color variations in the epidote. Fluid inclusions associated with crystal growth features (concentric zoning and crystal elongation) were assumed to be primary in origin. Primary fluid inclusions ranged in size from <1 to 10 μm in diameter. Secondary fluid inclusions were present in healed, curvilinear and irregular fractures that crosscut crystal growth features (Fig. 4B and
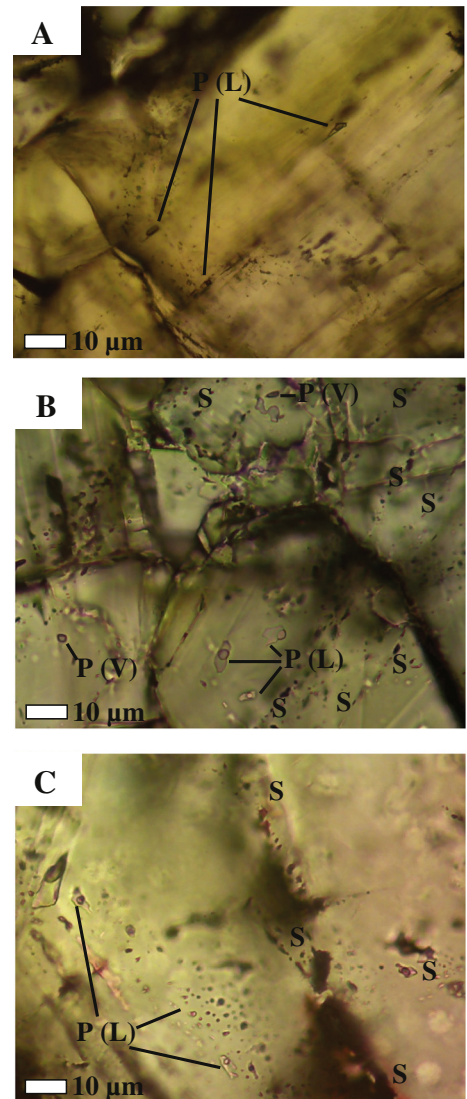
Fig. 4. (A through C) Transmitted light microphotographs of epidote-hosted fluid inclusions from 2799.15 m. (A) Primary vapor-rich fluid inclusion adjacent to wall rock. (B) Primary liquid and vapor fluid inclusions present inwards of the vein wall, shown here present in different crystals. (C) Liquid dominated fluid inclusions present in the vein center. P(V) = primary vapor inclusion; P(L) primary liquid inclusion; (S) = secondary inclusion.

C). Secondary fluid inclusions were <1 μm in diameter and not measurable. Both liquid and vapor rich fluid inclusions were present. The proportion of liquid to vapor varied according to the location of the epidote crystal hosting the fluid inclusion within the vein. Primary fluid inclusions adjacent to the vein wall typically had ~60% vapor, although a few were as low as ~30% vapor (Fig. 4A). Primary fluid inclusions inwards of the vein walls ranged from liquid dominated with ~30% vapor, to vapor dominated with almost the entire cavity filled by vapor (Fig. 4B). Vapor dominated fluid inclusions with >80% vapor volume could not be measured. Primary fluid inclusions in the vein center were liquid dominated with ~15 to 20% vapor.

T_h and T_m measurements were performed for fifty-seven epidote vein-hosted primary fluid inclusions (Table 1; Fig. 5). In some cases epidote crystals darkened on heating and T_h could not be observed, and in other cases fluid inclusions were too small to observe T_m. Calculated salinities for individual fluid inclusions ranged from 0.5 to 7.6 wt.% NaCl. T_h measurements for individual fluid inclusions ranged from 345 to >480 °C. A pressure correction for T_h measurements was evaluated based on the pressure equal to the hydrostatic head of a boiling water column at the depth of the samples, using experimental results for the two-phase boundary of seawater (Bischoff and Rosenbaur, 1985). The pressure at the depth of the RN-17B samples (~2560 m) was estimated to be approximately 185 bars. The trapping temperature (T_t) corrections of Potter (1977) are not well defined for the measured fluid inclusion T_h and salinity range, therefore fluid inclusion T_h results are reported uncorrected.

Calculated salinity values and T_h measurements of fluid inclusions followed a spatial pattern and fell into 3 categories that corresponded to fluid inclusion petrography: (1) a mixture of vapor-rich and liquid dominated inclusions with low salinity and T_h of 383.6 °C to 401.5 °C adjacent to vein walls; (2) a mixture of vapor and liquid dominated inclusions with low salinity and T_h > 480 °C inwards of the vein wall; and (3) liquid dominated fluid inclusions with T_h of 344.9 °C to 378.3 °C in vein centers with high salinities (Fig. 5). All three categories of fluid inclusions were present in the sample from 2798.64 m; only category 2 and 3 fluid inclusions were present in the sample from 2800.05 m.

4.3. Major element chemistry

EMP analyses of epidote are presented in Table 2. Vein epidote crystals are euhedral and generally compositionally zoned. Major element concentrations measured by EMP vary within each zone. Epidote analyses in Table 2 represent the centers of each epidote crystal where measured primary fluid inclusions occur. OH concentrations are not reported in Table 2, but they are included in the microprobe totals, as the number of OH ions is fixed at 2.0. The X_{Fe} of epidote hosting fluid inclusions ranged from 0.17 to 0.37. The X_{Fe} component in compositionally zoned epidote crystals is both normally (high X_{Fe} cores with low X_{Fe} rims) and reversely zoned, with no consistent spatial pattern. However, vein epidote adjacent to the wall rock has a higher aluminum concentration than the vein centers (Fig. 6).

EMP analyses of amphibole are presented in Table 3. Back-scattered electron (BSE) images reveal various morphologies of hydrothermal amphibole in the RN-17B core. Fine felted amphibole is present in chilled margins and crystalline edges of basalt fragments (Fig. 7A); larger, isolated amphibole crystals occur in the centers of basalt clast fragments (Fig. 7B), acicular amphibole occurs in the edges of vesicles (Fig. 7C) and veins, and coarse felted amphibole replaced hyaloclastite shards (Fig. 7D). Amphibole EMP analyses are corrected for ferric iron content according to the method of Dale et al. (2005). Results confirm that the amphibole is calcic and spans a compositional range from actinolitic hornblende to pargasitic hornblende (Fig. 8). Despite the green acicular, actinolitic appearance of amphibole in veins and vesicles, analyses confirm it is hornblendic in composition (Fig. 8). Amphibole analyses from the RN-17B core are consistent with amphibole analyses

Table 1
Epidote fluid inclusion measurements.

Epidote crystal/inclusion number	Sample depth	T_h (°C)	T_m (°C)	Salinity (wt.% NaCl)
1/1	2799.15	401.5	–	–
2/1	2799.15	400.4	–	–
3/1	2799.15	>480	–	–
4/1	2799.15	378.3	–	–
4/2	2799.15	–	−4.8	7.6
4/3	2799.15	–	−4.8	7.6
4/4	2799.15	–	−4.8	7.6
4/average		378.3	−4.8	7.6
5/1	2799.15	386.3	−1.1	1.9
6/1	2799.15	366.4	−3.3	5.4
6/2	2799.15	372	−3.2	5.3
6/average		369.2	−3.3	5.3
7/1	2799.15	390	−1.0	1.7
7/2	2799.15	–	−1.1	1.9
7/average		390	−1.1	1.8
8/1	2799.15	373.2	−2.8	4.6
8/2	2799.15	370	−3.3	5.4
8/average		371.6	−3.1	5.0
9/1	2799.15	372.9	−3.8	6.2
10/1	2799.15	385.9	−1.7	2.9
10/2	2799.15	385.8	−1.8	3.1
10/average		385.9	−1.8	3.0
11/1	2799.15	389.5	−0.6	1.1
12/1	2799.15	400.6	−2.4	4.0
12/2	2799.15	386.6	−2.5	4.2
12/3	2799.15	401.6	−1.7	2.9
12/average	2799.15	396.3	−2.2	3.7
13/1	2799.15	–	−0.9	1.6
14/1	2799.15	>480	−0.3	0.5
15/1	2799.15	400.1	–	–
15/2	2799.15	–	−0.6	1.1
15/average		400.1	−0.6	1.1
16/1	2799.15	370.4	−3.3	5.4
16/3	2799.15	–	−3.4	5.6
16/4	2799.15	370.6	−2.9	4.8
16/5	2799.15	369.7	–	–
16/6	2799.15	360.2	–	–
16/average		367.7	−3.2	5.3
17/1	2799.15	>480	−1.2	2.1
17/2	2799.15	>480	−1.4	2.4
17/3	2799.15	>480	−0.6	1.1
17/4	2799.15	>480	–	–
17/5	2799.15	>480	−1.5	2.6
17/average		>480	−1.2	2.0
18/1	2799.15	>480	−1.5	2.6
18/2	2799.15	>480	−1.2	2.1
18/3	2799.15	>480	−0.8	1.4
18/average		>480	−1.2	2.0
19/1	2799.15	>480	−1.4	2.4
19/2	2799.15	>480	–	–
19/average		>480	−1.4	2.4
20/1	2799.15	>480	−1.5	2.6
20/2	2799.15	>480	–	–
20/average		>480	−1.5	2.6
21/1	2800.05	344.9	−2.1	3.5
21/2	2800.05	358.1	−2.2	3.7
21/3	2800.05	354.2	−2.0	3.4
21/average		352.4	−2.1	3.5
22/1	2800.05	>480	−1.0	1.7
23/1	2800.05	>480	−0.9	1.6
24/1	2800.05	>480	−2.1	3.5
24/2	2800.05	>480	−2.0	3.4
24/average		>480	−2.1	3.5
25/1	2800.05	>480	−1.0	1.7
26/1	2800.05	>480	−0.8	1.4
26/2	2800.05	>480	–	–
26/3	2800.05	>480	−0.3	0.5
26/4	2800.05	>480	−1.0	1.7
26/5	2800.05	>480	−0.9	1.6
26/average		>480	−0.8	1.3
27/1	2799.15	354.3	−2.8	4.6
28/1	2799.15	352.2	−2.8	4.6

– Not measured due to small size, darkening, or decrepitation.
T_m ice melting temperature (°C).
T_h homogenization temperature (°C).

from RN-17 and RN-17B drill cuttings published by Marks et al. (2011), although RN-17B core samples do not span into actinolitic compositions along the pargasite exchange vector. Amphibole compositions vary spatially in a plagioclase–phyric clast with chilled margins from 2800.05 m (Figs. 7A, B, 8, and 9). Hornblende in the crystalline center of a clast from 2800.05 m is more actinolitic in composition than the outer crystalline edge of the clast, which is more hornblendic to pargasitic in composition. Hornblende in the altered quenched margin falls in between the compositions for the crystalline center and outer crystalline clast edge (Fig. 8). The Fe concentration is lower and the Mg concentration is higher for the altered quenched margin of the clast and altered hyaloclastite shards in the matrix than for the outer-most crystalline portions of the clast, while the crystalline center of the clast plots across a wide spectrum of FeO–MgO concentrations (Fig. 9).

EMP analyses of plagioclase are presented in Table 4, and representative plagioclase textures are presented on Fig. 10A through D. The majority of plagioclase analyses are biased toward plagioclase adjacent to hornblendic amphibole, which is predominantly very calcic, although two analyses of more sodic plagioclase were obtained. EMP analyses were performed on plagioclase in epidote vein selvedges present at 2799.90 and 2800.35 m (samples B-plag1 and 2; C-plag1, 2, and 3), relict igneous plagioclase laths present at 2804.30 m (samples F1-plag1 and 2), the center of an altered volcanic clast present at 2804.5 m (samples G2-plag1, 2, and 3), and the matrix between altered hyaloclastite shards present at 2804.80 m (samples H1-plag1, 2, 3 and 4; H2-plag1, 2, 3, and 4).

EMP analyses indicate that plagioclase compositions fall into two distinct groups: sodic plagioclase (An_{23} to An_{26}) and calcic plagioclase (An_{82} to An_{99}). The more sodic plagioclase appears darker in BSE images than the lighter calcic plagioclase. Hydrothermal plagioclase in veins and vein selvages was more calcic, and ranged from An_{86} to An_{98} (Fig. 10A). Relict igneous plagioclase, present in the crystalline cores of clasts, consists of intergrown calcic (An_{82}) and sodic plagioclase (An_{23}) and appears albitized in thin section and (Fig. 10B). Plagioclase in the core of an altered volcanic clast is calcic (An_{97} and An_{98}), and forms as an ~20 micron rim between a patch of chlorite and the surrounding hornblendic amphibole (Fig. 10C). Plagioclase present in the hyaloclastite matrix, adjacent to hyaloclastite shards altered to hornblende, consists of intergrown calcic (An_{85} to An_{99}) and sodic (An_{26}) plagioclase (Fig. 10D).

4.4. Strontium isotope chemistry

Results for $^{87}Sr/^{86}Sr$ epidote vein transects on a sample from 2800.05 m are presented in Fig. 11. Plagioclase phenocrysts in the Krafla glass fall in the expected $^{87}Sr/^{86}Sr$ ratio range of unaltered basalt (0.7030–0.7034; O'Nions and Grönvold, 1973; Sun and Jahn, 1975) and overlapped with the value of the sample (0.70328) determined from whole rock dissolution (Elders et al., 2011; Zierenberg et al., 2013). The DWC standard closely matched the expected $^{87}Sr/^{86}Sr$ ratio of seawater (0.7092; Dasch et al., 1973; Burke et al., 1982; Capo and DePaolo, 1992). The reproducibility of $^{87}Sr/^{86}Sr$ on varying substrates supports negligible matrix effects of the laser technique for epidote. $^{87}Sr/^{86}Sr$ ratios in epidote veins were higher on the vein edges (~0.70500) compared to the vein centers (~0.70400), and overlap the present-day strontium isotope composition of geothermal fluids from the Reykjanes Geothermal system (0.70412; Millot et al., 2009). The $^{87}Sr/^{86}Sr$ ratios in vein epidote from this study (Table 2; Fig. 11) are overall shifted toward seawater values, compared to basaltic values, consistent with measurements of epidote in drill cutting samples from RN-17 and RN-17B (Marks, 2010). Lower $^{87}Sr/^{86}Sr$ ratios in the vein centers are consistent with the presence of a second generation of epidote observed petrographically in vein centers throughout the RN-17B core (inner vein more yellow in color) and using back scattered electron (BSE) imaging (inner vein brighter and coarser texture). The signal intensity of ^{88}Sr increased coincident with the second generation of epidote, indicating a higher Sr concentration in the vein centers (Fig. 11).

Results for epidote crystals hosting fluid inclusions are overall shifted toward seawater $^{87}Sr/^{86}Sr$ values (Table 2), consistent with evolved seawater being trapped in both low salinity (<3.2 wt.% NaCl) and high salinity (>3.2 wt.% NaCl) fluid inclusions. No obvious spatial trend in $^{87}Sr/^{86}Sr$ was observed for these samples. This is possibly due to numerous wall rock and acicular green amphibole inclusions present in the samples from 2799.15 m. In contrast, the vein at 2800.05 m in which the epidote vein transects are measured has few wall rock or amphibole inclusions.

Marks (2010) found no relationship between the Sr concentration measured by EMP and the $^{87}Sr/^{86}Sr$ ratio measured by LA-MC-ICP-MS for drill cuttings from different depth intervals from RN-17B, or on the scale of individual zoned epidote grains. We found the same lack of correlation on the scale of individual epidote crystals present in veins.
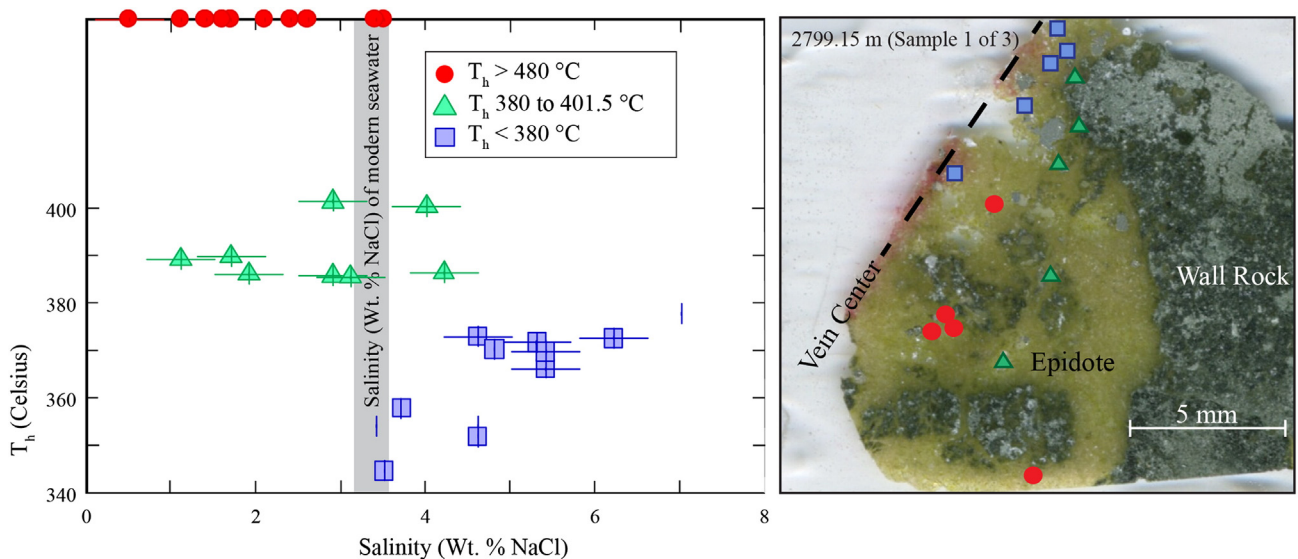

Fig. 5. Plot of T_h and salinity for fluid inclusions hosted by epidote veins from 2799.15 m and 2800.05 m (left). Error for $T_m = \pm 0.2$ °C, error for $T_h = \pm 5$ °C (see text for discussion). Spatial distribution of fluid inclusions at 2799.15 m (right).

Table 2

Electron microprobe analyses of epidote reported as oxides (all Fe as Fe_2O_3; based on 25 oxygens per formula unit) [upper]. $^{87}Sr/^{86}Sr$ determined using LA-MC-ICP-MS. Electron microprobe analyses of epidote reported as number of ions [lower].

Epidote crystal	Depth (m)	MgO	CaO	MnO	SrO	Al_2O_3	Fe_2O_3	SiO_2	TiO_2	Total	$^{87}Sr/^{86}Sr$
wt.% oxide											
2	2799.15	0.03	23.12	0.19	0.02	22.96	14.32	37.78	0.32	100.64	0.70437
3	2799.15	0.02	23.27	0.14	0.03	23.89	12.91	37.61	0.06	99.82	0.70449
5	2799.15	0.11	23.53	0.09	0.05	26.27	9.61	37.96	0.02	99.52	0.70457
7	2799.15	0.04	22.94	0.15	0.08	25.99	10.81	37.79	0.09	99.79	0.70475
8	2799.15	0.03	23.05	0.09	0.06	23.04	14.36	37.50	0.08	100.08	0.70511
9	2799.15	0.01	23.29	0.17	0.10	23.10	14.25	37.26	0.19	100.25	0.70568
10	2799.15	0.01	23.76	0.09	0.15	27.90	8.66	38.21	0.04	100.74	0.70456
11	2799.15	0.09	23.67	0.18	0.05	27.41	8.49	38.40	0.14	100.35	0.70449
12	2799.15	0.03	23.33	0.25	0.09	26.17	10.62	38.00	0.01	100.42	0.70464
13	2799.15	0.09	24.10	0.12	0.05	27.16	9.81	38.03	0.00	101.29	0.70441
14	2799.15	–	–	–	–	–	–	–	–		0.70453
15	2799.15	0.04	23.38	0.49	0.08	26.00	10.61	38.27	0.03	100.81	0.70418
16	2799.15	0.02	22.90	0.03	0.04	20.13	18.72	37.30	0.01	101.01	0.70438
17	2799.15	0.05	23.19	0.67	0.14	26.33	10.15	38.27	0.12	100.84	0.70428
18	2799.15	0.03	22.97	0.31	0.14	25.89	11.09	37.63	0.13	100.09	0.70469
19	2799.15	0.04	23.78	0.12	0.06	26.17	10.41	38.22	0.10	100.82	0.70468
20	2799.15	–	–	–	–	–	–	–	–		0.70471
21	2800.05	0.07	23.48	0.05	0.04	25.47	13.02	37.46	0.11	101.61	0.70474
23	2800.05	–	–	–	–	–	–	–	–		0.70457
24	2800.05	–	–	–	–	–	–	–	–		0.70466
25	2800.05	–	–	–	–	–	–	–	–		0.70490
26	2800.05	–	–	–	–	–	–	–	–		0.70478
27	2799.15	0.05	23.57	0.11	0.05	24.66	12.56	37.58	0.18	100.67	0.70465
28	2799.15	0.06	23.31	0.56	0.07	25.64	10.68	38.08	0.17	100.48	0.70421

Epidote crystal	Depth (m)	Mg	Ca	Mn	Sr	Al	Fe	Si	Ti	Total	X_{Fe}
Number of ions											
2	2799.15	0.01	3.93	0.03	0.002	4.29	1.71	5.99	0.04	17.98	0.28
3	2799.15	0.01	3.97	0.02	0.003	4.48	1.55	5.98	0.01	18.00	0.26
5	2799.15	0.03	3.97	0.01	0.005	4.88	1.14	5.98	0.00	18.01	0.19
7	2799.15	0.01	3.87	0.02	0.007	4.83	1.28	5.96	0.01	17.98	0.21
8	2799.15	0.01	3.93	0.01	0.005	4.33	1.72	5.98	0.01	17.99	0.28
9	2799.15	0.00	3.98	0.02	0.010	4.34	1.71	5.94	0.02	18.02	0.28
10	2799.15	0.00	3.95	0.01	0.013	5.10	1.01	5.93	0.01	18.02	0.17
11	2799.15	0.02	3.95	0.02	0.005	5.03	0.99	5.97	0.02	18.00	0.17
12	2799.15	0.01	3.92	0.03	0.008	4.83	1.25	5.95	0.00	18.00	0.21
13	2799.15	0.02	4.00	0.02	0.005	4.96	1.15	5.90	0.00	18.05	0.19
15	2799.15	0.01	3.91	0.07	0.007	4.79	1.25	5.98	0.00	18.00	0.21
16	2799.15	0.00	3.93	0.00	0.003	3.80	2.26	5.98	0.00	17.99	0.37
17	2799.15	0.01	3.88	0.09	0.013	4.84	1.19	5.97	0.01	18.00	0.20
18	2799.15	0.01	3.88	0.04	0.013	4.81	1.31	5.93	0.02	18.00	0.21
19	2799.15	0.01	3.97	0.02	0.006	4.81	1.22	5.96	0.01	18.01	0.20
21	2800.05	0.02	3.93	0.01	0.004	4.69	1.53	5.85	0.01	18.03	0.25
27	2799.15	0.01	3.98	0.01	0.004	4.58	1.49	5.92	0.02	18.02	0.25
28	2799.15	0.01	3.92	0.08	0.007	4.74	1.26	5.97	0.02	18.01	0.21

Analyses calculated on the basis of 25 oxygen structural formula.
OH fixed at an ion number of 2.00.
$^{87}Sr/^{86}Sr$ strontium isotope ratio determined by LA-ICP-MS.
$X_{Fe} = Fe/(Fe + Al)$.
– Not analyzed.
All Fe calculated as Fe_2O_3.

However, the signal intensity for ^{88}Sr measured by LA-MC-ICP-MS does appear to correlate with $^{87}Sr/^{86}Sr$ ratios in epidote vein transects (Fig. 11). The Neptune software Rb correction algorithm was not responsible for the higher ^{88}Sr signal in the later vein generation, as the measured ^{85}Rb intensity did not follow a similar pattern. The conflicting correlation between Sr signal intensity measured by LA-MC-ICP-MS and the Sr concentration measured by EMP may be due to heterogeneous distribution of Sr within individual epidote crystals. The smaller EMP spot size (1 μm) likely reflects Sr heterogeneity within single epidote crystals, while the larger (60 μm) LA-MC-ICP-MS spot size likely reflects the average Sr concentration in the crystals.

5. Discussion

The evidence for epidote paragenesis ranging from older on the vein edges to younger in the vein center is supported by three main lines of evidence. Different generations of epidote are apparent petrographically based on the variation in color and crystal morphology. Fluid inclusion homogenization temperatures and salinities in vein centers trend toward the current in-situ measured temperature (345 °C; Friðleifsson et al., 2011) and the modern salinity of Reykjanes fluids (Fig. 5). Additionally, the $^{87}Sr/^{86}Sr$ value of epidote in vein centers spans the $^{87}Sr/^{86}Sr$ of modern Reykjanes fluids (Fig. 11). Results from this study show systematic spatial geochemical variability in alteration minerals

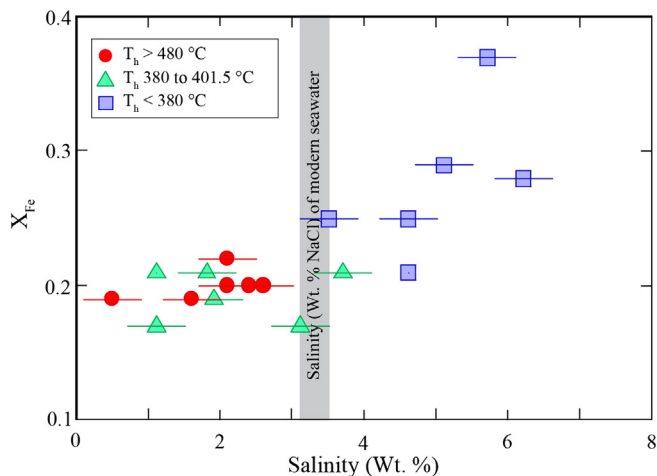**Fig. 6.** Mole fraction of Fe (X_{Fe} = Fe/Fe + Al) (y-axis) compared to salinity (x-axis) and temperature (legend symbols) in epidote crystals hosting fluid inclusions. Al is more concentrated in epidote that hosts lower salinity, higher temperature fluid inclusions, which are located adjacent to vein walls.

and indicate evolving temperature and fluid composition with time, accompanied by decreased water/rock ratio recorded by epidote veins in the RN-17B core. These results reflect changes over time in a very localized portion of the Reykjanes geothermal system. Our fluid inclusion and strontium isotope results for epidote in the RN-17B core are similar to fluid inclusions reported from Mid-Atlantic Ridge samples (Kelley and Delaney, 1987) and strontium isotope studies of core 504B from the East Pacific Rise (Alt et al., 1996; Teagle et al., 1998; Bach et al., 2003).

5.1. Geological setting

The lithologies present in the RN-17B core are characteristic of hyaloclastite deposits formed during submarine volcanic and subsequent epiclastic processes. Friðleifsson and Richter (2010) interpret the high vesicularity of some clasts, the formation of pillow lavas, and the presence of shell fragments as evidence for deposition of the lithologies in shallow marine conditions.

Several authors have attempted to link higher degrees of basalt vesicularity with lower hydrostatic pressure related to shallower seafloor depths (i.e. Moore, 1965, 1979; MacPherson, 1984). However, several samples of highly vesicular basalt have been recovered from seafloor depths of >4000 m in Hawaii (Clague et al., 1990), depths up to 3800 m on the Gorda mid-ocean ridge (Clague and Davis, 2003), depths of 1300 to >3400 m offshore central California (Davis and Clague, 2003), and depths between 400 and 1700 m on the Mid-Atlantic Ridge (Eissen et al., 2003; Fouquet et al., 2003). Results of these studies suggest that hydrostatic pressure of seawater alone is not sufficient to account for the degree of vesicularity observed in many types of deep submarine basalt. The CO_2 volatile component of basaltic magmas erupting on the seafloor likely determines the explosiveness and vesicularity of submarine eruptions (Davis and Clague, 2003; White et al., 2003). Also, observations at mid-ocean ridges indicate that the morphology of lava flows is related to the spreading rate (rather than hydrostatic pressure), with pillow lava formation favored at slow spreading ridges (Perfit and Chadwick, 1998). Therefore, the presence or absence of pillow lavas in the RN-17B core may not be a reliable indicator of eruption depth.

We suggest that the characteristics of the RN-17B core are not necessarily indicative of a shallow marine eruptive setting, and coupled with the great vertical depth (2500 m) of the drill core, may be indicative of deeper marine eruptive setting. Within the RN-17B core, Units 2 and 4 contain vesicular volcanic clasts with margins that appear quenched against the enclosing hyaloclastite matrix, indicating that the units are

preserved in situ. Fragmented clasts in Units 1 and 3 with quenched margins on only one side indicate slumping and redeposition, possibly in a debris-flow. Units 2, 3, 4, and 5 are all capped with crudely bedded volcanic sandstone, some with shell fragments and clasts with chilled margins on one side only, indicating epiclastic deposition.

Similar deep submarine deposits have been described for Pacific Ocean seamounts (Batiza et al., 1984), for the Mid-Atlantic Ridge (Schmincke et al., 1979), and for fossil seamounts in Hokkaido, Japan (Yamagishi, 1991). Batiza et al. (1984) described crudely bedded hyaloclastite deposits accumulating in depressions present at the crests of seamounts. Schmincke et al. (1979) argued that the Mid-Atlantic Ridge hyaloclastite deposits formed by a combination of pillows slumping on the sides of pillow basalt mounds and seawater currents preferentially carrying glass shards, sand-sized crystalline fragments, and clasts with chilled margins from rapidly erupting basalt and depositing them nearby. Yamagishi (1991) described epiclastic volcanic deposits on the flanks of fossil seamounts with crudely graded volcanic sand lithologies, interpreted to have formed during relatively quiescent interludes between eruptions.

An analogy for a likely depositional setting capable of creating the lithological features observed in the RN-17B core is the modern offshore portions of the Reykjanes Ridge. Parson et al. (1993) mapped submarine portions of the Reykjanes Ridge using high-resolution sidescan sonar, seismic profiles, and magnetic data. Parson et al. (1993) describe various morphologies of the submarine Reykjanes Ridge as a series of en echelon, 5 to 35 km long and 3 to 15 km wide axial volcanic ridges (AVRs) composed of overlapping volcanic edifices, often intersected by fault scarps trending between 0.5 km and 10 km long with vertical offsets up to 200 m. Parson et al. (1993) interpret the AVRs as having an early volcanic constructive period followed by a later, tectonically destructive period. Such a depositional setting could produce both the in situ eruptive units and re-deposited lithologies observed in RN-17B.

5.2. Fluid inclusions in epidote

Fluid inclusion T_h and salinity measurements from RN-17B (0.5–7.6 wt.% NaCl) are generally similar to those measured in ophiolite and ocean floor drillcore (i.e. Kelley and Delaney, 1987; Vanko, 1988; Nehlig, 1990; Vanko and Stakes, 1991; Kelley, 1997; Kelley and Früh-Green, 2001). However, several studies report fluid inclusion suites in seafloor hydrothermal systems from drill core with salinities up to and exceeding 50 wt.% NaCl (Kelley and Delaney, 1987; Vanko, 1988; Nehlig, 1990; Kelley, 1997; Kelley and Früh-Green, 2001). In comparison, the salinity of fluids expelled from active seafloor hydrothermal vents typically ranges from 40% less to 30% greater (~1.9 to 4.5 wt.% NaCl) than the 3.2 wt.% NaCl salinity of seawater (Bischoff and Rosenbaur, 1989; Nehlig, 1990 and references therein). Studies of seafloor hydrothermal systems commonly report some fluid inclusion suites with salinities less than the salinity of seawater (Kelley and Delaney, 1987; Vanko, 1988; Nehlig, 1990; Vanko and Stakes, 1991; Kelley, 1997; Kelley and Früh-Green, 2001), yet the geological setting precludes the possibility of meteoric recharge.

In terrestrial hydrothermal systems and shallow seafloor hydrothermal systems, fluid properties are generally governed by the two-phase boiling curve of hydrothermal fluids (Bischoff and Rosenbaur, 1985; Von Damm, 1995). Pressure conditions at oceanic spreading centers are typically in the range of ~200 to 750 bars, which corresponds to temperatures of 300 to 500 °C; spanning the critical point (298.5 bars and 407 °C) of seawater (Bischoff and Rosenbaur, 1988). Seawater crossing the two-phase boiling curve below the critical point under these conditions would produce a small amount of vapor with much lower concentrations of dissolved salts and metals than the liquid phase (Von Damm, 1995). In contrast, conditions in deep seafloor hydrothermal systems may well exceed the critical point of the hydrothermal fluid due to the large hydrostatic pressure resulting from the ocean mass (Bischoff and Rosenbaur, 1985). Seawater intersecting the

Table 3

Amphibole EMP analyses reported as oxides (all Fe as FeO; based on 23 oxygen formula) [upper]. Amphibole EMP analyses reported as number of ions (FeO recalculated as Fe^{2+} and Fe^{3+} using the method of Dale et al. (2005)) [lower].

All Fe is FeO based on 23 oxygen formula												
Amphibole sample	Depth (m)	# of analyses	SiO_2	Al_2O_3	TiO_2	MnO	MgO	CaO	Na_2O	K_2O	FeO	Total
wt.% oxide												
QE 1	2800.05	2	45.61	8.26	0.76	0.37	12.13	12.18	1.04	0.11	16.09	98.53
QE 2	2800.05	3	46.41	8.55	0.53	0.33	13.04	12.38	1.01	0.09	14.63	98.97
QE 3	2800.05	2	47.05	8.12	0.64	0.38	13.42	12.11	1.07	0.11	14.24	99.16
QE 4	2800.05	2	47.01	7.06	0.46	0.43	12.97	12.49	0.82	0.08	15.42	98.74
QE 5	2800.05	2	47.86	6.69	0.41	0.44	12.74	12.32	0.77	0.09	15.02	98.35
OC 1	2800.05	2	45.96	8.40	1.08	0.37	12.38	12.13	0.98	0.10	15.70	99.11
OC 2	2800.05	3	46.29	8.59	0.64	0.40	12.99	11.94	1.00	0.09	14.86	98.83
OC 3	2800.05	2	42.45	12.34	0.79	0.35	11.44	12.18	1.69	0.08	15.28	98.57
OC 4	2800.05	3	45.08	9.28	0.59	0.30	11.97	12.18	1.19	0.10	16.26	98.95
OC 5	2800.05	3	42.94	11.37	1.12	0.32	11.60	12.25	1.68	0.11	15.92	99.31
OC 6	2800.05	2	42.86	11.77	1.11	0.32	11.93	12.19	1.69	0.05	14.75	98.67
IC 1	2800.05	3	47.40	5.60	0.21	0.44	10.76	12.01	0.67	0.05	19.30	98.41
IC 2	2800.05	3	48.41	6.59	0.58	0.37	13.46	12.51	0.75	0.09	14.66	99.44
IC 3	2800.05	1	47.74	7.88	0.66	0.46	14.61	12.31	0.89	0.06	12.75	99.41
IC 4	2800.05	3	46.90	7.71	0.55	0.36	12.57	11.95	1.01	0.11	15.98	99.14
HS 1	2800.05	2	47.38	7.03	0.44	0.32	13.10	12.35	0.97	0.07	15.20	98.87
HS 2	2800.05	2	47.39	7.69	0.69	0.38	13.18	12.43	0.98	0.07	14.10	98.94
HS 3	2800.05	2	48.93	6.06	0.35	0.29	13.27	12.39	0.71	0.05	14.95	99.02
HS 4	2800.05	3	48.49	6.05	0.36	0.36	13.43	12.36	0.78	0.06	14.81	98.73
HS 5	2798.64	1	45.54	9.18	0.85	0.41	13.08	11.98	1.40	0.05	14.23	98.73
HS 6	2798.64	3	48.30	6.36	0.37	0.26	13.65	12.48	0.88	0.10	14.16	98.57
HS 7	2798.64	3	44.43	10.48	0.93	0.33	12.94	12.25	1.68	0.08	13.92	99.04
HS 8	2798.64	3	44.80	10.40	1.01	0.36	12.73	12.33	1.61	0.06	14.14	99.45
VS 1	2798.64	3	47.57	7.84	0.15	0.47	13.18	12.27	1.04	0.05	14.24	98.82
VS 2	2798.64	3	46.10	8.88	0.14	0.34	13.17	12.19	1.30	0.05	13.98	98.14
VS 3	2798.64	2	45.84	9.59	0.61	0.30	13.47	12.42	1.47	0.08	13.47	99.28
VS 4	2798.64	2	44.29	10.22	0.52	0.36	11.97	12.11	1.47	0.11	15.44	98.47
VS 5	2798.64	3	48.73	6.57	0.36	0.36	14.02	12.33	0.99	0.08	13.49	98.96
VS 6	2798.64	2	48.13	6.52	0.19	0.52	13.40	12.28	1.10	0.07	14.69	98.92
VS 7	2798.64	3	45.71	9.73	0.40	0.32	13.65	12.16	1.62	0.09	13.18	98.88
VS 8	2798.64	3	46.04	8.86	0.49	0.31	12.78	12.30	1.25	0.12	14.80	98.98
VS 9	2798.64	2	45.38	9.46	0.66	0.33	12.33	12.20	1.38	0.09	15.56	99.41
VE 1	2800.35	3	45.31	10.73	0.58	0.33	12.67	12.20	1.22	0.04	14.31	99.42
VE 2	2800.35	2	44.18	10.76	0.64	0.38	12.07	12.21	1.45	0.03	15.16	98.89
VE 3	2800.35	1	46.81	7.12	0.84	0.40	12.54	12.58	0.83	0.06	15.31	98.48
VE 4	2800.35	1	48.71	6.23	0.37	0.42	13.51	12.34	0.65	0.04	14.90	99.20
VE 5	2800.35	2	46.74	7.97	0.50	0.36	12.60	12.32	0.81	0.07	14.87	98.23
VE 6	2800.35	1	47.30	6.51	0.95	0.35	13.12	12.28	0.71	0.07	14.73	98.03
VE 7	2800.35	2	49.71	5.36	0.25	0.44	13.81	11.92	0.61	0.05	14.08	98.25

Amphibole sample	Si	Al	Ti	Mn	Mg	Ca	Na	K	Fe^{2+}	Fe^{3+}	Fe total	Sum	$Fe^{2+}/(Fe^{2+} + Mg)$
Number of ions													
QE 1	6.78	1.45	0.08	0.05	2.72	1.96	0.30	0.02	1.49	0.51	2.00	15.37	0.35
QE 2	6.82	1.48	0.06	0.04	2.89	1.97	0.29	0.02	1.31	0.48	1.80	15.35	0.31
QE 3	6.88	1.40	0.07	0.05	2.96	1.92	0.31	0.02	1.32	0.43	1.74	15.34	0.31
QE 4	6.94	1.23	0.05	0.05	2.89	2.00	0.24	0.02	1.36	0.55	1.90	15.31	0.32
QE 5	7.09	1.17	0.05	0.06	2.82	1.96	0.22	0.02	0.31	1.55	1.86	15.24	0.10
OC 1	6.78	1.46	0.12	0.05	2.75	1.94	0.29	0.02	1.45	0.48	1.94	15.34	0.35
OC 2	6.80	1.49	0.07	0.05	2.88	1.90	0.29	0.02	1.29	0.54	1.83	15.32	0.31
OC 3	6.32	2.16	0.09	0.04	2.59	1.96	0.49	0.02	1.36	0.54	1.90	15.57	0.34
OC 4	6.67	1.62	0.07	0.04	2.67	1.96	0.35	0.02	1.44	0.57	2.01	15.41	0.35
OC 5	6.36	1.98	0.12	0.04	2.59	1.97	0.49	0.02	1.42	0.56	1.97	15.56	0.35
OC 6	6.36	2.06	0.12	0.04	2.67	1.96	0.49	0.01	1.33	0.50	1.83	15.54	0.33
IC 1	7.14	0.99	0.02	0.06	2.44	1.96	0.20	0.01	1.95	0.48	2.43	15.25	0.44
IC 2	7.07	1.13	0.06	0.05	2.95	1.97	0.21	0.02	1.43	0.36	1.79	15.27	0.33
IC 3	6.91	1.34	0.07	0.06	3.19	1.93	0.25	0.01	1.07	0.48	1.54	15.30	0.25
IC 4	6.91	1.34	0.06	0.04	2.79	1.91	0.29	0.02	1.47	0.49	1.97	15.32	0.35
HS 1	6.98	1.22	0.05	0.04	2.91	1.97	0.28	0.01	1.44	0.43	1.87	15.34	0.33
HS 2	6.97	1.33	0.08	0.05	2.90	1.97	0.28	0.01	1.44	0.29	1.73	15.32	0.33
HS 3	7.18	1.05	0.04	0.04	2.92	1.96	0.20	0.01	1.52	0.32	1.84	15.24	0.34
HS 4	7.14	1.05	0.04	0.05	2.97	1.97	0.22	0.01	1.46	0.36	1.82	15.27	0.33
HS 5	6.71	1.59	0.09	0.05	2.90	1.91	0.40	0.01	1.31	0.44	1.75	15.43	0.31
HS 6	7.11	1.10	0.04	0.03	3.02	1.98	0.25	0.02	1.42	0.32	1.74	15.30	0.32
HS 7	6.54	1.82	0.10	0.04	2.87	1.95	0.48	0.01	1.28	0.43	1.71	15.53	0.31
HS 8	6.58	1.80	0.11	0.04	2.81	1.96	0.46	0.01	1.36	0.37	1.74	15.50	0.33
VS 1	6.99	1.36	0.02	0.06	2.91	1.95	0.30	0.01	1.42	0.33	1.75	15.34	0.33
VS 2	6.82	1.55	0.02	0.04	2.93	1.95	0.38	0.01	1.29	0.43	1.73	15.42	0.31
VS 3	6.70	1.65	0.07	0.04	2.96	1.96	0.42	0.02	1.26	0.39	1.65	15.47	0.30
VS 4	6.59	1.79	0.06	0.05	2.68	1.95	0.43	0.02	1.42	0.50	1.92	15.49	0.35
VS 5	7.13	1.13	0.04	0.04	3.07	1.94	0.28	0.01	1.39	0.26	1.65	15.31	0.31

Table 3 (continued)

Amphibole sample	Si	Al	Ti	Mn	Mg	Ca	Na	K	Fe^{2+}	Fe^{3+}	Fe total	Sum	$Fe^{2+}/(Fe^{2+} + Mg)$
VS 6	7.09	1.13	0.02	0.07	2.96	1.95	0.32	0.01	1.50	0.31	1.81	15.36	0.34
VS 7	6.70	1.68	0.04	0.04	3.01	1.93	0.46	0.02	1.21	0.41	1.62	15.50	0.29
VS 8	6.78	1.54	0.05	0.04	2.83	1.96	0.36	0.02	1.40	0.43	1.82	15.42	0.33
VS 9	6.68	1.64	0.07	0.04	2.73	1.95	0.40	0.02	1.44	0.48	1.92	15.45	0.34
VE 1	6.61	1.85	0.06	0.04	2.79	1.93	0.35	0.01	1.24	0.51	1.75	15.38	0.31
VE 2	6.53	1.87	0.07	0.05	2.69	1.96	0.42	0.01	1.35	0.52	1.87	15.47	0.33
VE 3	6.94	1.24	0.09	0.05	2.80	2.02	0.24	0.01	1.46	0.44	1.90	15.30	0.34
VE 4	7.12	1.07	0.04	0.05	2.97	1.95	0.19	0.01	1.40	0.42	1.82	15.23	0.32
VE 5	6.93	1.39	0.06	0.05	2.81	1.97	0.23	0.01	1.44	0.40	1.84	15.29	0.34
VE 6	7.02	1.14	0.11	0.04	2.93	1.97	0.21	0.01	1.44	0.39	1.83	15.26	0.33
VE 7	7.31	0.93	0.03	0.06	3.05	1.89	0.17	0.01	1.45	0.28	1.73	15.18	0.32

QE = quenched edge (clast edge).
OC = outer crystalline (inwards of quenched edge).
IC = inner crystalline (clast center).
HS = hyaloclastite shard.
VS = acicular green amphibole in vesicles.
VE = acicular green amphibole in vein selvedges
FeO recalculated as Fe^{2+} and Fe^{3+} using the method of Dale et al. (2005).

two-phase region from above the critical point would remain mostly in the vapor phase and condense a small amount of dense brine (Bischoff and Rosenbaur, 1985; Von Damm, 1995). This model fits fluid inclusion evidence from seafloor hydrothermal systems (Bischoff and Rosenbaur, 1985; Kelley and Delaney, 1987; Nehlig, 1990; Vanko and Stakes, 1991; Kelley, 1997; Kelley and Früh-Green, 2001). Some authors have also suggested that the formation of saline brines in seafloor hydrothermal systems can be attributed to direct exsolution of fluids from cooling magma, although direct evidence of this has not been reported (Kelley and Früh-Green, 2001 and references therein).

Fluid inclusion homogenization temperatures and the hydrostatic pressure at the depth of the RN-17B core suggest that the critical point of seawater was not exceeded. Any phase separation of hydrothermal fluids in the Reykjanes system is likely the result of the liquid to vapor phase transition of seawater below the critical point, thus we would not expect to see highly saline fluid inclusions at the depth of the RN-17B core. A key difference between the Reykjanes geothermal system and seafloor hydrothermal systems is that significantly greater depth is required at Reykjanes to approach similar hydrostatic pressure conditions seen in seafloor hydrothermal systems. This is a consequence of the cold hydrostatic pressure of overlying ocean water present in seafloor systems being absent in the Reykjanes system, which instead has a pressure regime dictated by the hot hydrostatic pressure of seawater.

The spatial relationships in RN-17B epidote veins – specifically that the least saline fluid inclusions are found adjacent to wall rocks as opposed to vein interiors – imply that Category 1 inclusions formed during the earliest stage of epidote precipitation. The low salinities of Category 1 inclusions are less than and approaching the salinity of seawater, and T_h exceeds the temperature of the two-phase boundary for seawater at the estimated hydrostatic pressure for boiling seawater at the sample depth (Fig. 12). These results suggest an early stage of boiling due to increased temperatures during the initial formation of the epidote veins.
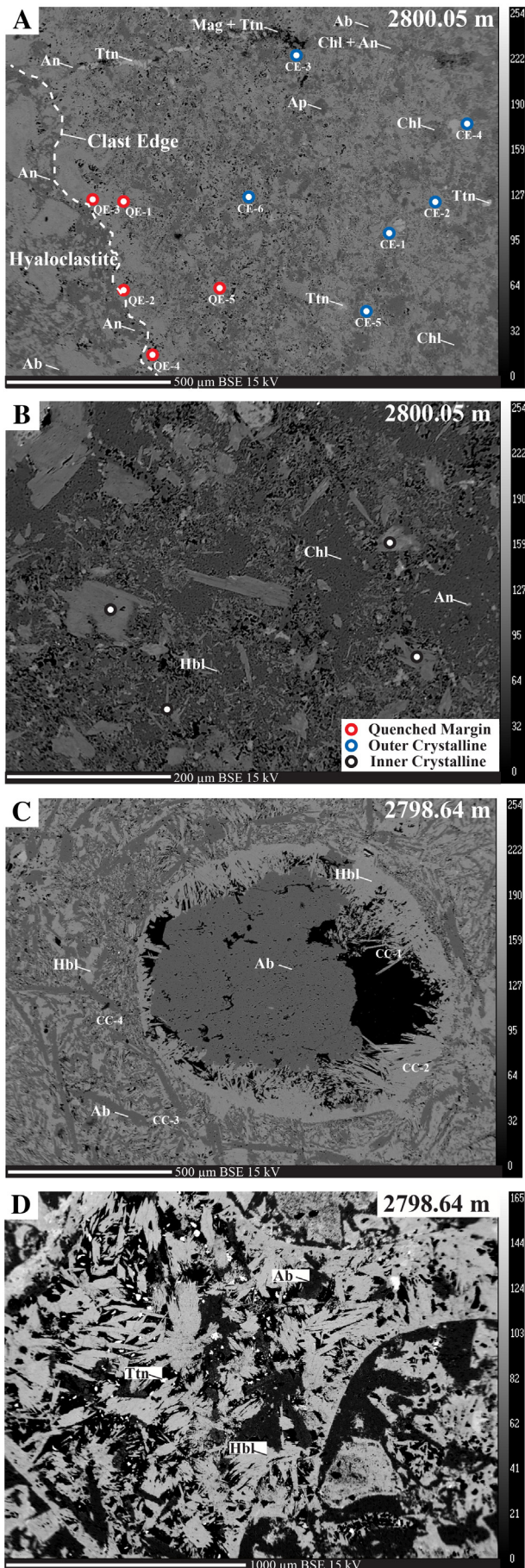
Non-homogenizing fluid inclusions (Category 2 inclusions) exhibit salinities approaching seawater, but will not homogenize below the maximum attempted temperature of 480 °C. No evidence of decrepitation or the presence of CO_2 was observed, however, the small size of fluid inclusions could possibly obscure the presence of a secondary liquid phase. Anomalous fluid inclusions trapping liquid plus steam effervescing through liquid due to boiling at greater depth would produce $T_h > T_t$ (Roedder, 1984). Evidence for boiling in adjacent, earlier Category 1 fluid inclusions provides support for interpretation of non-homogenizing fluid inclusions forming as a result of boiling seawater below the critical point.

Category 3 inclusions are present in vein centers and formed during the final stages of vein precipitation. Category 3 inclusions are liquid dominated, have higher salinities than seawater, and lower homogenization temperatures than paragenetically earlier fluid inclusions. Temperatures in Category 3 inclusions trend toward the most recently measured downhole temperature in RN-17B (345 °C; Friðleifsson et al., 2011). These inclusions possibly trapped a slightly more saline liquid residue formed from boiling of a liquid with a significant seawater component. This hypothesis is also supported by the fact that homogenization temperatures for the more saline Category 3 fluid inclusions fall below the boiling curve (Fig. 12).

Fluid inclusions trapped during the filling of epidote veins in the RN-17B core appear to record an episode of boiling seawater followed by incursion of a more saline residue. Initial boiling is preserved in Category 1 fluid inclusions based on the presence of vapor-rich fluid inclusions with salinities less than that of seawater. Continued boiling is preserved in Category 2 fluid inclusions, which will not homogenize, indicating the presence of two primary fluid phases (steam and liquid) trapped out of equilibrium. A later cooler, more saline residue is preserved in the liquid-dominated Category 3 fluid inclusions. Our fluid inclusion T_h and salinity measurements indicate that epidote veins in the RN-17B core record an episode of boiling and subsequent cooling below the two-phase boundary for RN-17B hydrothermal fluids.

Fluid inclusion results from epidote veins in the RN-17B core are remarkably similar to those reported by Kelley and Delaney (1987) for altered gabbro samples recovered from the western median valley walls of the Mid-Atlantic Ridge near 24°N. Kelley and Delaney (1987) reported an early episode of brittle fracture recorded by fluid inclusions in apatite with homogenization temperatures of 400 °C and salinities of 1–2 wt.% NaCl. Kelley and Delaney (1987) concluded that brittle fracture was followed by sealing of the fracture network due to incursion of lower temperature fluids recorded by fluid inclusions in plagioclase, apatite, epidote, and augite with homogenization temperatures of 200–300 °C and salinities of 1–7 wt.% NaCl.

Franzson et al. (2002) described a similar range in fluid inclusion salinities for calcite, quartz and plagioclase at shallower depths (526 to 1338 m) in wells RN-9 and RN-10 in the Reykjanes geothermal system. Fluid inclusion temperatures for calcite at 526 m in RN-10 measured by Franzson et al. (2002) showed a T_h range of ~170 °C to 250 °C, however this study was completed on drill cutting samples, so interpretation of paragenetic relationships of fluid inclusions was not attempted. In the nearby Svartsengi geothermal field, Franzon (1990) concluded from fluid inclusion data that the geothermal system had cooled by 10 to 20 °C at 800 m, and by ~50 °C at 1350 m depth. Franzon (1990) also noted that fluid inclusion salinities became more

Fig. 7. (A through D) BSE images reveal various amphibole morphologies present in the RN-17B core. Red, blue, and black circles indicate the locations of EMP analyses presented in Fig. 8. Abbreviations: Ab = albite, An = anorthite, Ap = apatite, Chl = chlorite, Hbl = hornblende, Mag = magnetite, Ttn = titanite. (For interpretation of the references to color in this figure legend, the reader is referred to the web version of this article.)
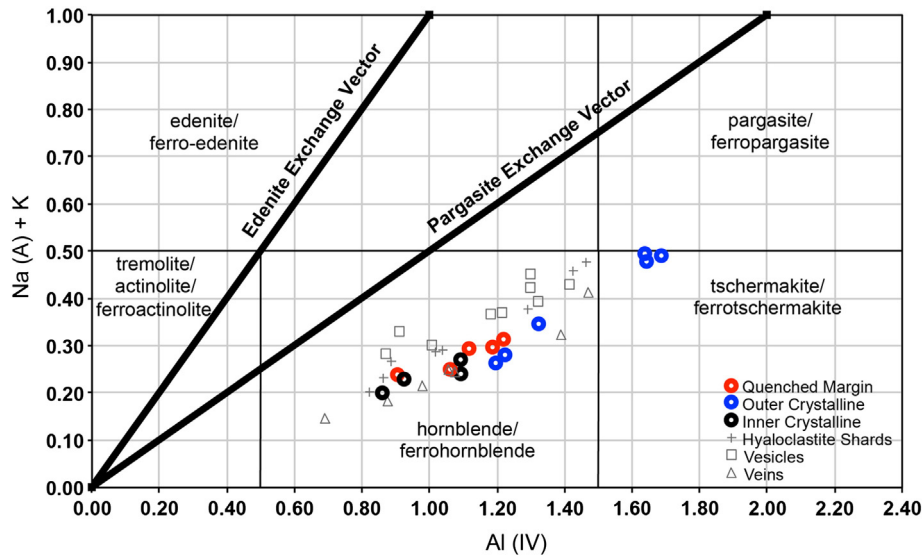
saline with time at Svartsengi. Franzson interpreted the range in fluid inclusion properties from the Reykjanes and Svartsengi geothermal systems as evidence for fluid evolution from fresh to seawater due to meteoric water recharge from a regional icecap present during the last glaciation. Fluid inclusions from the RN-17B core indicate a salinity increase and cooling of ~55 °C at a vertical depth of 2560 m, consistent with Franzson's model. An alternative model is that low salinity fluid inclusions reported by Franzson et al. (2002) are related to phase separation of seawater, an idea supported by the proximity of the fluid inclusion homogenization temperatures to the boiling point–depth curve for seawater (Fig. 12). In situations where fluids are near the two-phase boundary, rapid fracture dilation can result in localized isenthalpic phase separation, brine formation, cooling, and supersaturation of mineral phases (Henley and Hughes, 2000). Our very localized fluid inclusion and strontium isotope results do not preclude meteoric recharge in shallower portions of the Reykjanes geothermal system, although are consistent with phase separation of seawater similar to that reported for many submarine hydrothermal systems.

One explanation for boiling at the depth of the RN-17B core may be a period of elevated temperatures due to injection of a dike or dike swarm. Preliminary examination of the nearby RN-30 core shows evidence of several dikes with chilled margins at a similar vertical depth to the RN-17B core (~2200 m in RN-30 vs 2560 m in RN-17B). Despite no evidence for meteoric water recharge at the depth of the RN-17B core, our results do not preclude the influence of an icecap on the Reykjanes geothermal system. Boiling at shallow depths may have been influenced by the removal of an icecap, which would possibly result in an initial pressure decrease followed by a temperature decrease once the temperature gradient re-equilibrated with the displaced boiling–depth curve.

5.3. Epidote composition

Epidote zoned with respect to Fe^{3+}–Al^{3+} is commonly formed in hydrothermal systems hosted in a variety of geological settings (Bird et al., 1984; Arnason and Bird, 1992; Bird and Spieler, 2004). Fluid flux, permeability, temperature, oxygen fugacity (fO_2), carbon dioxide fugacity (fCO_2), fluid pH, whole rock composition, and aqueous speciation of Al^{3+} and Fe^{3+} are important variables controlling epidote composition (Arnason and Bird, 1993; Bird and Spieler, 2004). Temperature, fCO_2, and fO_2 are the most important intensive variables controlling epidote composition, however elucidation of the key variable is generally not possible (Arnason and Bird, 1993).

Experimental studies have demonstrated the influence of temperature on the Fe^{3+} content of epidote, and show that the relationship is strongly dependent on the buffering mineral assemblage (Apted and Liou, 1983; Liou et al., 1983; Arnason and Bird, 1993). The Fe content of epidote is highly sensitive to small fluctuations in fCO_2 in H_2O-rich fluids with overall low fCO_2, although again, the relationship is strongly dependent on the buffering mineral assemblage (Arnason and Bird, 1993). The Fe^{3+} content of epidote appears to be directly related to fO_2; oxidized mineral assemblages contain the most Fe-rich epidote, while reduced assemblages contain the most Fe-poor epidote (Holdaway, 1972; Bird and Helgeson, 1981; Liou et al., 1983; Arnason and Bird, 1993; Bird and Spieler, 2004).

EMP analyses of epidote from drill cuttings in wells RN-8 and RN-9 in the Reykjanes geothermal system and wells in the nearby Svartsengi geothermal system show no systematic changes in major element concentration with depth or proximity of aquifers, despite documentation of many grains having complex zoning patterns (Lonker et al., 1993;

Fig. 8. Spatially resolved amphibole compositions are consistent with those presented by Marks et al. (2011), however variations in amphibole composition in the RN-17B core relate to protolith permeability and composition. Microprobe totals recalculated using the method of Dale et al. (2005). (For interpretation of the references to color in the text, the reader is referred to the web version of this article.)

Bird and Spieler, 2004). There are no systematic changes in X_{Fe} of epidote with depth or temperature in RN-17 cuttings (Freedman et al., 2009; Marks et al., 2010). Epidote in RN-17 drill cuttings from 2000 to 3000 m depth shows no Al–Fe (III) zoning, and X_{Fe} ranges from 0.17 to 0.36 (Freedman et al., 2009). The results of this study show a comparable range of X_{Fe} in epidote from a single epidote vein at 2799.15 m in the RN-17B core (X_{Fe} of 0.17 to 0.37) compared to drill cuttings from the entire depth of RN-17 and other locations in the Reykjanes and Svartsengi geothermal systems. However, the X_{Fe} of epidote grain centers appears to have changed systematically during the infilling of the epidote vein (Fig. 6). In contrast to drill cutting results reported by Freedman et al. (2009) for RN-17 between 2000 and 3000 m depth, vein epidote in the RN-17B core commonly has oscillatory zoning with respect to Al–Fe (III), although the zoning within individual crystals shows no systematic pattern.

The systematic change in X_{Fe} of epidote in the RN-17B core shows little correlation with T_h of fluid inclusions, consistent with the results of Marks et al. (2010) for epidote in drill cuttings compared with depth and temperature. There appears to be a consistent relationship between salinity of fluid inclusions and X_{Fe} of the host epidote (Fig. 6). The reported strong dependence of epidote composition on fO_2 suggests
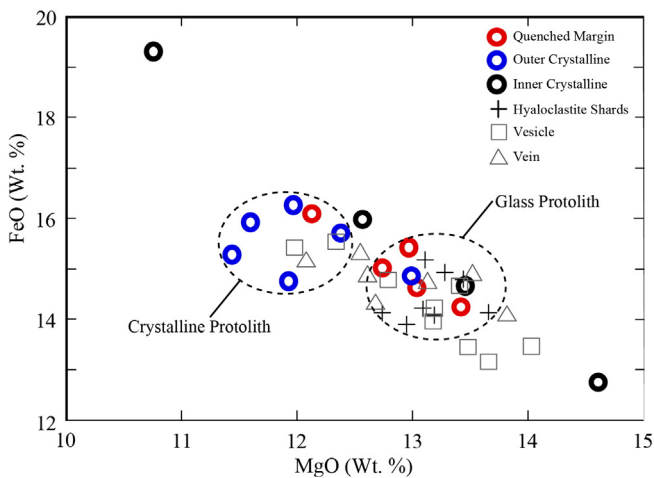

Fig. 9. Fe and Mg concentrations of amphiboles vary according to protolith type with glass protoliths showing higher MgO contents.

Table 4
Plagioclase EMP analyses reported as wt.% oxides [upper]. Plagioclase EMP analyses reported as number of ions [lower].

Plagioclase sample	Depth (m)	Na₂O	K₂O	CaO	Fe₂O₃	Al₂O₃	SiO₂	Total
Wt.% oxide								
B-plag1	2799.90	0.21	0.00	20.04	0.34	36.01	42.88	99.48
B-plag2	2799.90	0.17	0.01	20.36	1.25	34.67	41.91	98.37
C-plag1	2800.35	0.96	0.03	17.82	1.00	34.12	43.30	97.22
C-plag2	2800.35	1.47	0.02	17.03	0.41	33.45	44.73	97.10
C-plag3	2800.35	1.52	0.04	16.93	0.78	33.40	44.92	97.58
F1-plag1	2804.30	2.07	0.05	16.65	0.28	33.47	47.11	99.64
F1-plag2	2804.30	9.12	0.07	4.80	0.23	23.62	62.71	100.54
G2-plag1	2804.50	0.21	0.01	19.39	0.84	36.11	42.54	99.11
G2-plag2	2804.50	0.33	0.02	19.54	0.51	35.69	42.78	98.86
G2-plag3	2804.50	0.23	0.00	19.87	0.45	36.38	43.15	100.08
H1-plag1	2804.80	0.09	0.01	20.21	0.48	36.93	42.48	100.19
H1-plag2	2804.80	1.17	0.04	17.40	0.85	33.80	44.45	97.70
H1-plag3	2804.80	0.33	0.02	19.62	0.60	35.76	43.09	99.42
H1-plag4	2804.80	1.45	0.01	17.49	1.20	32.78	46.06	98.99
H2-plag1	2804.80	1.66	0.00	17.62	0.51	34.07	45.75	99.60
H2-plag2	2804.80	1.26	0.02	18.27	0.46	34.85	45.34	100.20
H2-plag3	2804.80	8.47	0.07	5.52	0.08	24.33	61.27	99.74
H2-plag4	2804.80	1.12	0.02	18.08	0.25	34.90	45.29	99.66

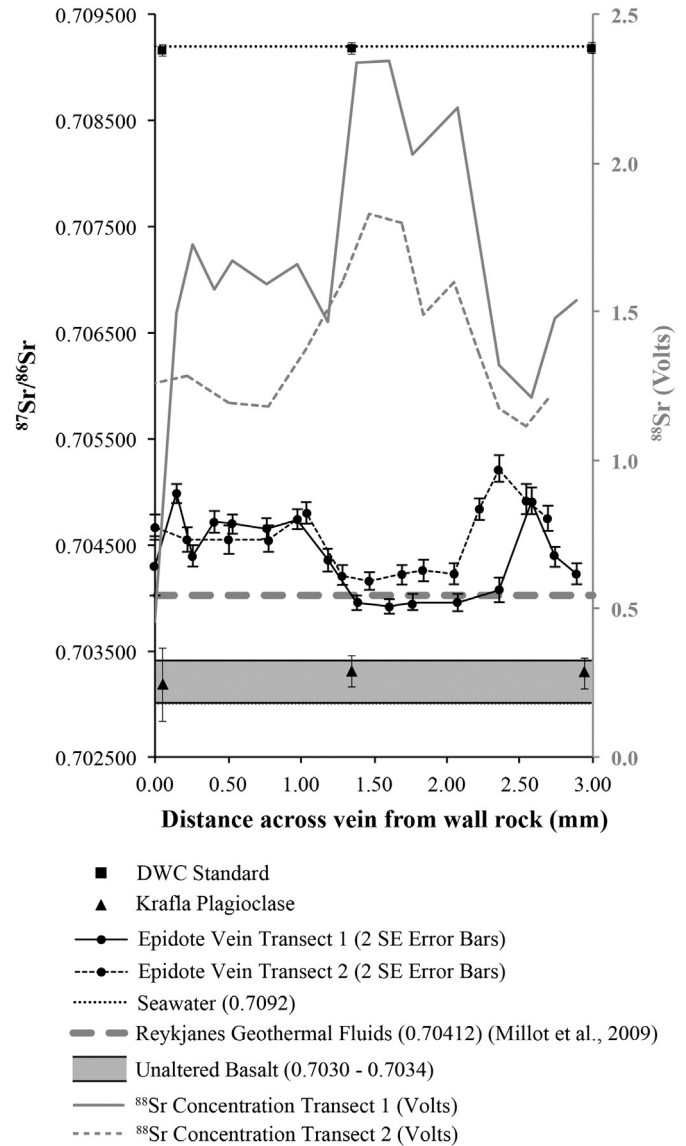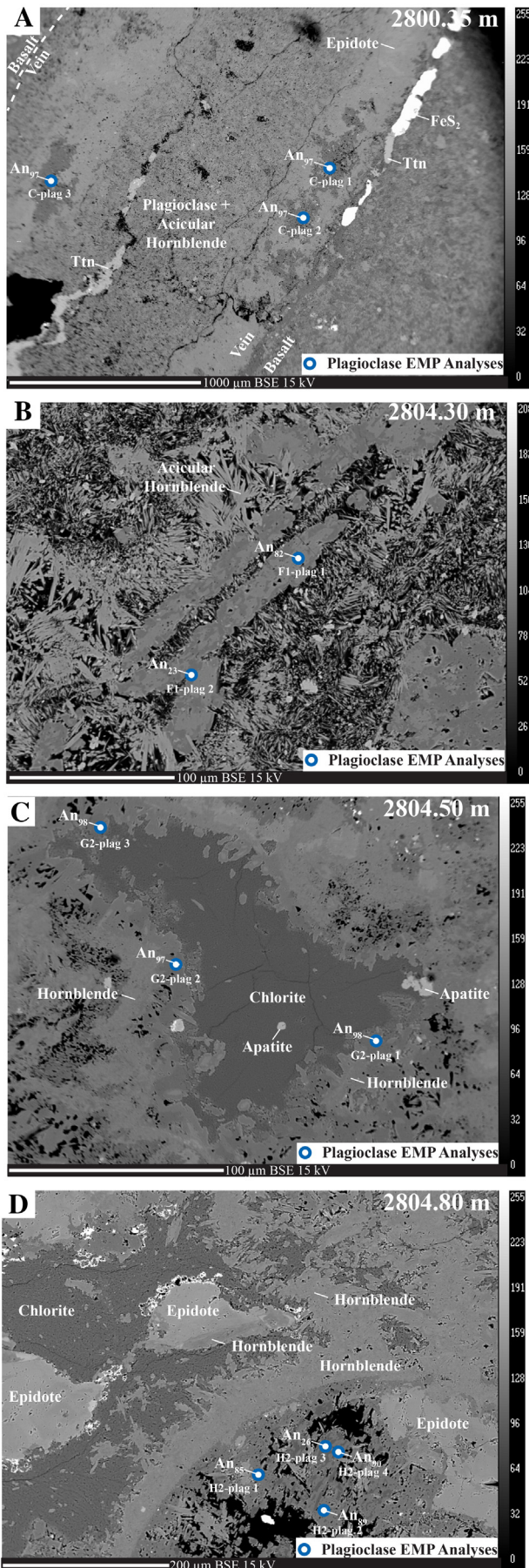| Plagioclase sample	Depth (m)	Na	K	Ca	Fe	Al	Si	Total	An content
Number of Ions									
B-plag1	2799.90	0.02	0.00	1.00	0.01	1.98	2.00	5.01	98
B-plag2	2799.90	0.02	0.00	1.04	0.05	1.94	1.99	5.03	98
C-plag1	2800.35	0.09	0.00	0.91	0.04	1.91	2.06	5.01	91
C-plag2	2800.35	0.14	0.00	0.87	0.01	1.87	2.12	5.01	87
C-plag3	2800.35	0.14	0.00	0.86	0.03	1.86	2.12	5.01	86
F1-plag1	2804.30	0.19	0.00	0.82	0.01	1.82	2.17	5.01	82
F1-plag2	2804.30	0.78	0.00	0.23	0.01	1.23	2.77	5.01	23
G2-plag1	2804.50	0.02	0.00	0.97	0.03	1.99	1.99	5.01	98
G2-plag2	2804.50	0.03	0.00	0.98	0.02	1.97	2.01	5.01	97
G2-plag3	2804.50	0.02	0.00	0.99	0.02	1.99	2.00	5.01	98
H1-plag1	2804.80	0.01	0.00	1.00	0.02	2.02	1.97	5.02	99
H1-plag2	2804.80	0.11	0.00	0.88	0.03	1.88	2.10	5.00	89
H1-plag3	2804.80	0.03	0.00	0.98	0.02	1.97	2.01	5.01	97
H1-plag4	2804.80	0.13	0.00	0.87	0.04	1.80	2.15	5.00	87
H2-plag1	2804.80	0.15	0.00	0.87	0.02	1.86	2.12	5.02	85
H2-plag2	2804.80	0.11	0.00	0.90	0.02	1.89	2.09	5.01	89
H2-plag3	2804.80	0.73	0.00	0.26	0.00	1.28	2.73	5.00	26
H2-plag4	2804.80	0.10	0.00	0.90	0.01	1.90	2.09	5.01	90

An content = Ca/(Ca + Na) ∗ 100.

Fig. 11. Two LA-ICP-MS transects of an epidote vein at 2800.05 m. The ^{88}Sr signal (Sr abundance) increases in the vein center, and the $^{87}Sr/^{86}Sr$ ratio decreases in the vein center.

that fluid salinity changes were occurring contemporaneously with evolving fO_2 in the geothermal system during vein sealing, rather than salinity being the independent variable, if fO_2 is in fact the controlling variable for the X_{Fe} of epidote in this case. A potential explanation for evolving fO_2 may be partitioning of reduced gasses, primarily H_2S and H_2, into the vapor phase during boiling that could have left the residual more saline liquid more oxidized. High concentrations of H_2S (26.5% by volume) and H_2 (28.1% by volume) are present in geothermal gas emissions at the Nesjavellir Power Plant, Iceland (Balta et al., 2010), which supports the idea that these gasses may be present in a geothermal system at sufficient concentrations to affect the fO_2 of geothermal fluids at depth. Alternatively, a variation in fluid flux may be the controlling factor for the X_{Fe} of epidote in the RN-17B core, an idea consistent with the mineralization of epidote and subsequent decrease in permeability.

Sealing of permeability and the related shift to lower fluid–rock ratios may explain the systematic change in X_{Fe} across epidote veins.

Fig. 10. (A through D) BSE images and EMP analyses reveal that hydrothermal plagioclase is calcic (A and C), while altered igneous plagioclase in the hyaloclastite matrix consists of intergrown calcic and sodic plagioclase (B and D). Abbreviations as in Fig. 7; FeS$_2$ = pyrite.
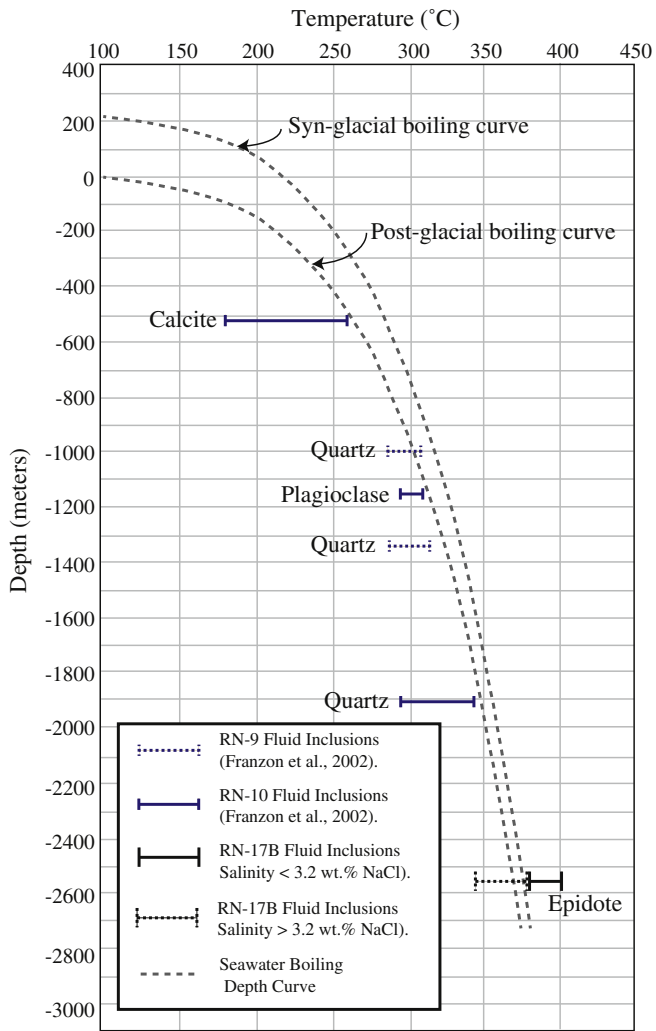
Fig. 12. Reykjanes geothermal system fluid inclusion temperatures in relation to the boiling–depth curve for seawater.
Modified after Franzson et al. (2002) and Marks et al. (2010).

Lower fluid–rock ratios are consistent with a reduced flux of hydrothermal fluid able to transport dissolved Al from plagioclase in the wall rock (i.e. Alt and Emmerman, 1985; Alt, 1995). Mobilization of Al for incorporation into the epidote structure may occur during albitization of calcic plagioclase and/or breakdown of chlorite in the wall rock. Subsequent solutions may have lower Al content possibly due to the fluid being isolated from the wall rock by earlier precipitated Al-rich epidote and/or Al-rich amphibole, thus precipitating more Fe-rich epidote. Alternatively, boiling would increase the pH of fluids and influence the relative proportions of Fe^{3+} and Al^{3+} in solution, although thermodynamic modeling is required to determine if the reduction of Fe^{3+} or Al^{3+} would be larger.

5.4. Amphibole and plagioclase major element compositions

Despite the pervasive amphibolite grade alteration in the RN-17B core, original textures are preserved, including hyaloclastite glass shards, lithic clasts, and chilled margins of clasts and pillow basalts. Transition from greenschist assemblages to higher-grade amphibolite assemblages is defined in part by replacement of actinolite with hornblende, and the presence of calcic plagioclase. EMP analyses of hydrothermal amphibole reveal that centers of pillow basalt fragments (black rings, Fig. 6) plot closer to the actinolitic end of the pargasite exchange vector. The crystalline cores of pillow basalt fragments retain

greenschist grade minerals such as chlorite, and contain sparse, isolated hydrothermal hornblende crystals. The outermost crystalline edges of the pillow fragments (blue rings, Fig. 7) are predominantly composed of felted hornblende and plot closer to the aluminous end of the pargasite exchange vector. These results reflect evolution of amphibole composition from actinolitic to pargasitic with increasing water/rock ratios. Protolith type (glass or crystalline) also appears to contribute to the composition of amphiboles. EMP analyses of quenched glassy margins on the pillow basalt (red rings, Fig. 8) plot closer to actinolitic compositions than analyses from crystalline parts of the pillow would predict. Amphibole FeO/MgO ratios also suggest that protolith composition controls on amphibole composition (Fig. 9). Glass protoliths (hyaloclastite shards and quenched clast margins) have higher Mg and lower Fe concentrations than fragments with crystalline protolith, possibly due to enrichment in Mg from earlier palagonitization or chloritization of the glass. The exception to this is hornblende in the very center of crystalline protolith fragments, which spans the entire range of Fe/Mg ratios for crystalline and glass protoliths.

Hydrothermal amphibole and calcic plagioclase have been described previously in mafic rocks from mid-ocean ridge hydrothermal systems (i.e. Alt et al., 1985, 1986, 1996; Vanko and Stakes, 1991; Gillis and Thompson, 1993; Alt, 1995). Amphibole compositions in seafloor hydrothermal systems commonly change with increasing depth and temperature from actinolite to Mg-hornblende with corresponding increases in Al and Ti contents (Gillis and Thompson, 1993; Alt, 1995). A similar pattern is observed in the results from this study corresponding to the extent of fluid "seen" by the protolith (Figs. 8 and 9). Fig. 8 indicates an increasing Al content for amphibole in crystalline basalt from the center of a pillow toward the edge of the pillow, while Fig. 9 indicates an increase in Mg from the crystalline portion of a basalt pillow toward the glassy margin of the pillow. Overall, EMP results for amphibole indicate that alteration in the RN-17B core has not reached equilibrium in part due to limited permeability. However, timing of alteration events coupled with evolving fluid compositions, and localized chemical controls may also contribute to the systematic variability observed in amphibole compositions.

5.5. Strontium isotope ratios in epidote

Strontium isotope fractionation is not temperature or mineral dependent, and $^{87}Sr/^{86}Sr$ ratios are significantly different for fresh volcanic rock and seawater (Alt et al., 1996). The low Rb concentration and the young age (<1 Ma) of Reykjanes basalts preclude significant radiogenic ^{87}Sr contamination in samples (Marks et al., 2010). For these reasons $^{87}Sr/^{86}Sr$ ratios are particularly useful for evaluating fluid–rock interaction in seawater dominated geothermal systems, and have been used previously to evaluate seawater influence on epidote precipitation in seafloor hydrothermal systems (i.e. Alt et al., 1996) and epidote from drill cuttings in the Reykjanes geothermal system (Marks et al., 2010).

$^{87}Sr/^{86}Sr$ measurements of epidote from RN-17 and RN-17B drill cuttings, in addition to three powdered samples of RN-17B core whole-rock do not vary with depth or alteration grade, but do vary with increased loss on ignition (LOI) (Marks et al., 2010). Our results show that lower $^{87}Sr/^{86}Sr$ ratios in vein centers are shifted toward rock values, consistent with the possibility that epidote veins in the RN-17B core record evolution to lower water/rock ratios. Such a relationship between $^{87}Sr/^{86}Sr$ ratios and water/rock ratio has been demonstrated previously in whole rock studies of seafloor hydrothermal systems (i.e. Kawahata et al., 1987). Evolving conditions to lower water/rock ratios is consistent with epidote precipitation and a subsequent decrease in water/rock ratio in the fracture network of the RN-17B core due boiling hydrothermal fluids. Conversely, the Sr concentration in epidote is higher in the centers of epidote veins (based on the increased voltage for ^{88}Sr) as measured by LA-MC-ICP-MS (Fig. 11). This observation is in contrast to the relationship

observed by Kawahata et al. (1987) for decreasing water/rock ratios in a seafloor hydrothermal system where Sr content remained steady while the $^{87}Sr/^{86}Sr$ ratios decreased. Assumedly, lower water/rock ratios would accompany a decrease in Sr content obtained by fluids precipitating epidote due to decreased exposure to the surrounding host rock. However, if the fluids precipitating epidote in vein centers resulted from phase separation and concentration of dissolved solids into a liquid phase due to boiling, a process indicated by our fluid inclusion measurements, fluids in vein centers may have had a higher Sr content than the more dilute fluids forming epidote on the vein edges. Such a partitioning of Sr into a brine or liquid phase has been suggested previously (Bach and Humphris, 1999).

Salinities lower than seawater in fluid inclusions have previously been interpreted as evidence for evolution from freshwater to seawater fluids in shallow portions of the Reykjanes geothermal system (i.e. Franzon, 1990; Franzson et al., 2002). The implication for the overall seawater $^{87}Sr/^{86}Sr$ values in vein epidote is that earlier, less saline hydrothermal fluids had a significant component of seawater. Dilution of 3.2 wt.% NaCl seawater by freshwater to get salinities as low as the ~1 wt.% NaCl we see in the RN-17B core epidote veins would require greater than 3:1 dilution by freshwater and would result in lower overall Sr content, something that is observed (Fig. 11). However, this degree of dilution by freshwater at an early stage of epidote vein formation would assumedly shift $^{87}Sr/^{86}Sr$ values toward rock values and we see the opposite trend (Fig. 11). Therefore, strontium isotope transects across epidote veins suggest that an early meteoric water history for the Reykjanes geothermal system is not recorded by epidote veins in the RN-17B core.

6. Conclusions

A key difference between the seawater dominated Reykjanes geothermal system and seafloor hydrothermal systems is the lack of cold hydrostatic seawater head. Subsequently, significantly greater depths are required at Reykjanes before temperatures, pressures and mineralization similar to those observed in seafloor hydrothermal systems are observed. The ~2560–2570 m vertical depth of the RN-17B core bears many similarities in terms of fluid inclusion characteristics, alteration mineral phases, and alteration mineral compositions as seen in submarine hydrothermal systems. Future recovery of deeper core from the Reykjanes Peninsula may give insights into hydrothermal processes in the deep ocean crust, particularly if depths exceeding the critical point of seawater are achieved.

This geochemical investigation of samples from drill core RN-17B has revealed evolving geothermal conditions in the Reykjanes geothermal system, evaluated utilizing in situ geochemical methods on drill core as opposed to drill cuttings. Fluid inclusion evidence suggests cooling over time of Reykjanes geothermal fluids (below the critical point for seawater) from above the two-phase boundary to below the two-phase boundary. Fluid inclusion salinities indicate that cooling appears to be accompanied by fluids composed of low salinity vapor evolving to more saline residual brine. The Al content of epidote measured by EMP suggests that the cooling of the system is accompanied by sealing of permeability in the geothermal system, supported by strontium isotope ratios measured in epidote vein transects using LA-MC-ICP-MS. Strontium isotope ratios also indicate that hydrothermal fluids had a significant seawater component throughout precipitation of epidote and sealing of permeability in veins. Therefore, incursion of low salinity meteoric fluids is not required to explain fluid inclusion salinities less than seawater at the depth of the RN-17B core. The Al and Mg contents of hydrothermal amphibole measured by EMP suggest that amphibole compositions are related to protolith type and water–rock ratio, and indicate that alteration mineralogy in the RN-17B core has not reached equilibrium in part due to water–rock ratio and in part due to the glassy versus crystalline nature of the protolith.

Appendix A. Supplementary data

Supplementary data to this article can be found online at http://dx. doi.org/10.1016/j.jvolgeores.2015.06.009.

References

Alt, J.C., 1995. Subseafloor processes in mid-ocean ridge hydrothermal systems. In: Humphris, S.E., Zierenberg, R.A., Mullineaux, L.S., Thomson, R.E. (Eds.), Seafloor Hydrothermal Systems: Physical, Chemical, Biological, and Geological Interactions, Geophysical Monograph vol. 91. AGU, Washington, pp. 85–113.

Alt, J.C., Emmerman, R., 1985. Geochemistry of hydrothermally altered basalts— deep sea drilling project hole 504B, leg 83. In: Anderson, J., Honnorez, J., Becker, K., et al. (Eds.), Initial Reports, DSDP vol. 83. US Government Printing Office, Washington, pp. 249–262.

Alt, J.C., Laverne, C., Muehlenbachs, K., 1985. Alteration of the upper oceanic crust— mineralogy and processes in deep sea drilling project hole 504B, leg 83. In: Anderson, J., Honnorez, J., Becker, K., et al. (Eds.), Initial Reports, DSDP vol. 83. US Government Printing Office, Washington, pp. 217–247.

Alt, J.C., Honnorez, J., Laverne, C., Emmerman, R., 1986. Hydrothermal alteration of a 1 km section through the upper oceanic crust, deep sea drilling project hole 504B: mineralogy, chemistry, and evolution of seawater basalt intrusions. J. Geophys. Res. 91 (B10), 10,309–310,335.

Alt, J.C., Teagle, D.A.H., Bach, W., Halliday, A.N., Erzinger, J., 1996. Stable and strontium isotopic profiles through hydrothermally altered upper oceanic crust, hole 504B. Proc. Ocean Drill. Program Sci. Results 148.

Apted, M.J., Liou, J.G., 1983. Phase relations among greenschist epidote–amphibolite, and amphibolite in a basalt system. Am. J. Sci. 283-A, 328–354.

Armbruster, T., Bonazzi, P., Akasaka, M., Bermanec, V., Chopin, C., Gieré, R., Heuss-Assbichler, S., Liebscher, A., Menchetti, S., Pan, Y., Pasero, M., 2006. Recommended nomenclature of epidote-group minerals. Eur. J. Mineral. 18 (5), 551–567.

Arnason, J.G., Bird, D.K., 1992. Formation of zoned epidote in hydrothermal systems. Proceedings Proc. 7th International Symposium on Water–Rock Interaction, Park City, Utah, pp. 1473–1476.

Arnason, J.G., Bird, D.K., 1993. Variables controlling epidote composition in hydrothermal and low-pressure regional metamorphic rocks. Proceedings Abhand Geol. Bund., Salzburg, Austria vol. 49, pp. 17–25.

Arnórsson, S., 1978. Major element chemistry of the geothermal sea-water at Reykjanes and Svartsengi, Iceland. Mineral. Soc. 42 (322), 209–220.

Arnórsson, S., 1995. Geothermal systems in Iceland — structure and conceptual models — I. High temperature areas. Geothermics 24 (5/6), 561–602.

Bach, W., Humphris, S.E., 1999. Relationship between the Sr and O isotope compositions of hydrothermal fluids and the spreading and magma-supply rates at oceanic spreading centers. Geology 27 (12), 1067.

Bach, W., Peucker-Ehrenbrink, B., Hart, S.R., Blusztajn, J.S., 2003. Geochemistry of hydrothermally altered oceanic crust: DSDP/ODP Hole 504B — implications for seawater-crust exchange budgets and Sr- and Pb-isotopic evolution of the mantle. Geochem. Geophys. Geosyst. 4, 1–29.

Balta, M.T., Dincer, I., Hepbasli, A., 2010. Potential methods for geothermal-based hydrogen production. Int. J. Hydrog. Energy 35, 4949–4961.

Batiza, R., Fornari, D.J., Vanko, D.A., Lonsdale, P., 1984. Craters, calderas, and hyaloclastites on young Pacific seamount. J. Geophys. Res. 89 (B10), 8371–8390.

Bird, D.K., Helgeson, H.C., 1981. Chemical interaction of aqueous solutions with epidote-feldspar mineral assemblages in geologic systems— II. Equilibrium constraints in metamorphic geothermal processes. Am. J. Sci. 281, 576–614.

Bird, D.K., Spieler, A.R., 2004. Epidote in geothermal systems. Rev. Mineral. 56, 235–300.

Bird, D.K., Schiffman, P., Elders, W.A., Williams, A.E., McDowell, D., 1984. Calc-silicate mineralization in active geothermal systems. Econ. Geol. 79, 671–695.

Bischoff, J.L., Rosenbaur, R.J., 1985. An empirical equation of state for hydrothermal seawater (3.2 percent NaCl). Am. J. Sci. 285, 725–763.

Bischoff, J.L., Rosenbaur, R.J., 1988. Liquid–vapor relations in the critical region of the system NaCl–H₂O from 380 to 415 °C: a refined determination of the critical point and two-phase boundary of seawater. Geochim. Cosmochim. Acta 52, 2121–2126.

Bischoff, J.L., Rosenbaur, R.J., 1989. Salinity variations in submarine hydrothermal systems by layered double-diffusive convection. J. Geol. 97 (5), 613–623.

Bodnar, R.J., 1993. Revised equation and table for determining the freezing point depression of H₂O–NaCl solutions. Geochim. Cosmochim. Acta 57, 683–684.

Burke, W.H., Denison, R.E., Hetherington, E.A., Koepnick, R.B., Nelson, H.F., Otto, J.B., 1982. Variation of seawater $^{87}Sr/^{86}Sr$ throughout Phanerozoic time. Geology 10 (10), 516.

Capo, R.C., DePaolo, D.J., 1992. Homogeneity of Sr isotopes in the oceans. EOS Trans. Am. Geophys. Union 73, 272.

Clague, D.A., Davis, A.S., 2003. Submarine strombolian eruptions on the Gorda mid-ocean ridge in explosive submarine volcanism. In: White, J.D.L., Smellie, J.L., Clague, D.A. (Eds.), American Geophysical Union, Geophysical Monograph 140, Washington D.C., pp. 111–128

Clague, D.A., Holcomb, R.T., Sinton, J.M., Detrick, R.S., Torresan, M.E., 1990. Pliocene and Pleistocene alkalic flood basalts on the seafloor north of the Hawaiian islands. Earth Planet. Sci. Lett. 98, 175–191.

Clifton, A.E., Kattenhorn, S.A., 2006. Structural architecture of a highly oblique divergent plate boundary segment. Tectonophysics 419 (1–4), 27–40.

Dale, J., Powell, R., White, R.W., Elmer, F.L., Holland, T.J.B., 2005. A thermodynamic model for Ca–Na clinoamphiboles in Na_2O–CaO–FeO–MgO–Al_2O_3–SiO_2–H_2O–O for petrological calculations. J. Metamorph. Geol. 23 (8), 771–791.

Dasch, J.E., Hedge, C.E., Dymond, J., 1973. Effect of sea water interaction on strontium isotope composition of deep-sea basalts. Earth Planet. Sci. Lett. 19 (2), 177–183.

Davis, A.S., Clague, D.A., 2003. Hyaloclastite from Miocene seamounts offshore central California: compositions, eruption styles, and depositional processes in explosive submarine volcanism. In: White, J.D.L., Smellie, J.L., Clague, D.A. (Eds.), American Geophysical Union, Geophysical Monograph 140, Washington D.C., pp. 129–141

Eissen, J., Fouquet, Y., Hardy, D., Ondreas, H., 2003. Recent MORB volcaniclastic explosive deposits formed between 500 and 1750 m.b.s.l on the axis of the Mid-Atlantic Ridge, south of the Azores in explosive submarine volcanism. In: White, J.D.L., Smellie, J.L., Clague, D.A. (Eds.), American Geophysical Union, Geophysical Monograph 140, Washington D.C., pp. 143–166

Elders, W.A., Friðleifsson, G.O., Zierenberg, R.A., Pope, E.C., Mortensen, A.K., Guðmundsson, A., Lowenstern, J.B., Marks, N.E., Owens, L., Bird, D.K., Reed, M., Olsen, N.J., Schiffman, P., 2011. Origin of a rhyolite that intruded a geothermal well while drilling at the Krafla volcano, Iceland. Geology 39 (3), 231–234.

Fouquet, Y., Eissen, J., Ondreas, H., Barriga, F., Batiza, R., Danyushevsky, L., 2003. Extensive volcaniclastic deposits at the Mid-Atlantic Ridge axis—results of deep-water basaltic explosive activity? Terra Nova 10, 280–286.

Franzon, H., 1990. Svartsengi. Geological model of a high temperature system and its surroundings. Orkustofnun Report OS-90050:JHD-08 (41 pp., in Icelandic with English summary).

Franzson, H., Thordarson, S., Bjornsson, G., Gudlaugsson, S., Richter, B., Friðleifsson, G.Ó., Thorhallsson, S., 2002. Reykjanes high-temperature field, SW-Iceland. Geology and hydrothermal alteration of well RN-10. 27th Stanford Workshop on Geothermal Reservoir Engineeringpp. 233–240.

Freedman, A.J.E., Bird, D.K., Arnorsson, S., Fridriksson, T., Elders, W.A., Fridleifsson, G.O., 2009. Hydrothermal minerals record CO_2 partial pressures in the Reykjanes geothermal system, Iceland. Am. J. Sci. 309 (9), 788–833.

Friðleifsson, G., Elders, W., 2005. The Iceland Deep Drilling Project: a search for deep unconventional geothermal resources. Geothermics 34 (3), 269–285.

Friðleifsson, G.Ó., Richter, B., 2010. The geological significance of two IDDP-ICDP spot cores from the Reykjanes Geothermal Field, Iceland. Proceedings World Geothermal Congress 2010 Bali, Indonesia, 25–29 April 2010pp. 1–7.

Friðleifsson, G.O., Blischke, A., Reyr, B.K., Richter, B., Einarsson, G.M., Jónasson, H., Franzson, H., Sigurðsson, Ó., Danielsen, P.E., Jónsson, S.S., Thordarson, S., Þórhallsson, S., Harðardóttir, V., Egilson, O., 2005. Reykjanes Well Report RN-17 and RN-17ST, ISOR-2005/007. Iceland Geosurvey, Reykjavik.

Friðleifsson, G.Ó., Albertsson, A., Elders, W., Sigurdsson, Ó., Karlsdottir, R., Pálsson, B., 2011. The Iceland Deep Drilling Project (IDDP): planning for the second deep well at Reykjanes. Geotherm. Resour. Counc. Trans. 35, 347–354.

Gillis, K.M., Thompson, G., 1993. Metabasalts from the Mid-Atlantic Ridge— new insights into hydrothermal systems in slow-spreading crust. Contrib. Mineral. Petrol. 113, 502–523.

Helgadóttir, H.M., Gunnarsdóttir, S.H., Guðfinnsson, G.H., Ingólfsson, H., 2009. Reykjanes — Well RN-17B, Drilling the Production Part of the Well 933 to 3077 m. ÍSOR-2009/008 (154 pp. & Appendix, in Icelandic).

Henley, R.W., Hughes, G.O., 2000. Underground fumaroles: "excess heat" effects in vein formation. Econ. Geol. 95, 453–466.

Holdaway, M.J., 1972. Thermal stability of Al–Fe epidote as a function of fO_2 and Fe content. Contrib. Mineral. Petrol. 37, 307–340.

Ildefonse, B., Rona, P.A., Blackman, D., 2007. Drilling the crust at mid ocean ridges. Oceanography 20, 66–77.

Jakobsson, S.P., Jonsson, J., Shido, F., 1978. Petrology of the Western Reykjanes Peninsula, Iceland. J. Petrol. 19 (4), 669–705.

Kawahata, H., Kusakabe, M., Kikuchi, Y., 1987. Strontium, oxygen, and hydrogen isotope geochemistry of hydrothermally altered and weathered rocks in DSDP Hole 504B, Costa Rica Rift. Earth Planet. Sci. Lett. 85, 343–355.

Kelley, D.S., 1997. Fluid evolution in slow-spreading environment. Proc. Ocean Drill. Program Sci. Results 153, 399–415.

Kelley, D.S., Delaney, J.R., 1987. Two-phase separation and fracturing in mid-ocean ridge gabbros at temperatures greater than 700 °C. Earth Planet. Sci. Lett. 83, 53–66.

Kelley, D.S., Früh-Green, G.L., 2001. Volatile lines of descent in submarine plutonic environments— insights from stable isotope and fluid inclusion analyses. Geochim. Cosmochim. Acta 65 (19), 3325–3346.

Kristmannsdóttir, H., 1975. Hydrothermal alteration of basaltic rocks in Icelandic geothermal areas. Proceedings of the 2nd U.N. Symposium on the Development and Use of Geothermal Resources, San Francisco, pp. 441–445.

Liou, J.G., Kim, H.S., Maruyama, S., 1983. Prehnite–epidote equilibria and their petrologic applications. J. Petrol. 24 (4), 321–342.

Lonker, S.W., Franzon, H., Kristmannsdottir, H., 1993. Mineral fluid interactions in the Reykjanes and Svartsengi geothermal systems. Am. J. Sci. 293, 605–670.

MacPherson, G.J., 1984. A model for predicting the volumes of vesicles in submarine basalts. J. Geol. 92 (1), 73–82.

Marks, N., 2010. Hydrothermal Alteration and Contact Metamorphism in the Reykjanes Geothermal System: Implications for Fluid–Rock Interactions at Mid-oceanic Ridge Spreading Centers (Ph.D. Dissertation). University of California Davis.

Marks, N., Schiffman, P., Zierenberg, R., Franzson, H., Fridleifsson, G., 2010. Hydrothermal alteration in the Reykjanes geothermal system: insights from Iceland Deep Drilling Program well RN-17. J. Volcanol. Geotherm. Res. 189, 172–190.

Marks, N., Schiffman, P., Zierenberg, R.A., 2011. High-grade contact metamorphism in the Reykjanes geothermal system: implications for fluid–rock interactions at mid-oceanic ridge spreading centers. Geochem. Geophys. Geosyst. 12 (8).

Millot, R., Ásmundsson, R., Négrel, P.H., Sanjuan, B., Bullen, T.D., 2009. Multi-isotopic (H, O, C, S, Li, B, Si, Sr, Nd) approach for geothermal fluid characterization in Iceland. Geochim. Cosmochim. Acta Suppl. 73, 883.

Moore, J.G., 1965. Petrology of deep-sea basalt near Hawaii. Am. J. Sci. 263, 40–52.

Moore, J.G., 1979. Vesicularity and CO_2 in mid-ocean ridge basalt. Nature 282, 250–253.

Nehlig, P., 1990. Salinity of oceanic hydrothermal fluids— a fluid inclusion study. Earth Planet. Sci. Lett. 102, 310–325.

Ólafsson, J., Riley, J.P., 1978. Geochemical studies on the thermal brine from Reykjanes, Iceland. Chem. Geol. 21 (3–4), 219–237.

O'Nions, R.K., Grönvold, K., 1973. Petrogenetic relationships of acid and basic rocks in Iceland; Sr-isotopes and rare-earth elements in late and postglacial volcanics. Earth Planet. Sci. Lett. 19 (4), 397–409.

Parson, L.M., Murton, B.J., Searle, R.C., Booth, D., Evans, J., Field, P., Keeton, J., Laughton, A., McAllister, E., Millard, N., Redbourne, L., Rouse, I., Shor, A., Smith, D., Spencer, S., Summerhayes, C., Walker, C., 1993. En echelon axial volcanic ridges at the Reykjanes Ridge: a life cycle of volcanism and tectonics. Earth Planet. Sci. Lett. 117, 73–87.

Perfit, M.R., Chadwick, W., 1998. Magmatism at mid-ocean ridges: constraints from volcanological and geochemical investigations in faulting and magmatism at Mid-Ocean Ridges. In: Roger Buck, W., Delaney, Paul T., Karson, Jeffrey A., Lagabrielle, Yves (Eds.), American Geophysical Union, Geophysical Monograph 106, Washington D.C., pp. 59–115

Pope, E., Bird, D., Arnórsson, S., Fridriksson, T., Elders, W., Fridleifsson, G., 2009. Isotopic constraints on ice age fluids in active geothermal systems: Reykjanes, Iceland. Geochim. Cosmochim. Acta 73, 4468–4488.

Potter, R.W., 1977. Pressure corrections for fluid-inclusion homogenization temperatures based on the volumetric properties of the system $NaCl$–H_2O. U.S. Geol. Surv. J. Res. 5, 603–607.

Roedder, E., 1984. Fluid inclusions. Mineralogical Society of America. Rev. Mineral. 12.

Sæmundsson, K., 2011. Geological map of western Reykjanes Peninsula 1:50,000. ISOR and HS Orka hf.

Schmincke, H.U., Robinson, P.T., Ohnmacht, W., Flower, M.F.J., 1979. Basaltic hyaloclastites from hole 396B, DSDP leg 46. DSDP Report vol. XLVI, pp. 341–348.

Spooner, E.T.C., 1974. Sub-seafloor metamorphism, heat and mass transfer; an additional comment. Contrib. Mineral. Petrol. 45, 169–173.

Spooner, E.T.C., Fyfe, W.S., 1973. Sub-seafloor metamorphism, heat and mass transfer. Contrib. Mineral. Petrol. 42, 287–304.

Sun, S.S., Jahn, B., 1975. Lead and strontium isotopes in post-glacial basalts from Iceland. Nature 255, 527–530.

Sveinbjörnsdóttir, A.E., Coleman, M.L., Yardley, B.W.D., 1986. Origin and history of hydrothermal fluids of the Reykjanes and Krafla geothermal fields, Iceland. Contrib. Mineral. Petrol. 94 (1), 99–109.

Teagle, D.A.H., Alt, J.C., Halliday, A.N., 1998. Tracing the chemical evolution of fluids during hydrothermal recharge: constraints from anhydrite recovered in ODP Hole 504B. Earth Planet. Sci. Lett. 155, 167–182.

Tómasson, J., Kristmannsdóttir, H., 1972. High temperature alteration minerals and thermal brines, Reykjanes, Iceland. Contributions to Mineralogy and Petrology 36, 123–134.

Vanko, D.A., 1988. Temperature, pressure, and composition of hydrothermal fluids, with their bearing on the magnitude of tectonic uplift at mid-ocean ridges, inferred from fluid inclusions in oceanic layer 3 rocks. J. Geophys. Res. 93 (B5), 4595–4611.

Vanko, D.A., Stakes, D.S., 1991. Fluids in oceanic layer 3: evidence from veined rocks, hole 735B, Southwest Indian Ridge. Proc. Ocean Drill. Program Sci. Results 118, 181–215.

Von Damm, K.L., 1995. Controls on the chemistry and temporal variability of seafloor hydrothermal fluids. In: Humphris, S.E., Zierenberg, R.A., Mullineaux, L.S., Thomson, R.E. (Eds.), Seafloor Hydrothermal Systems: Physical, Chemical, Biological, and Geological Interactions, Geophysical Monograph vol. 91. AGU, Washington, pp. 222–246.

White, J.D.L., Smellie, J.L., Clague, D.A., 2003. A deductive outline and topical overview of subaqueous explosive volcanism in explosive submarine volcanism. In: White, J.D.L., Smellie, J.L., Clague, D.A. (Eds.), American Geophysical Union, Geophysical Monograph 140, Washington D.C., pp. 1–23

Yamagishi, H., 1991. Morphological and sedimentological characteristics of the Neogene submarine coherent lavas and hyaloclastites in Southwest Hokkaido, Japan. Sediment. Geol. 74 (1–4), 5–23.

Zierenberg, R.A., Schiffman, P., Barfod, G.H., Lesher, C.E., Marks, N.E., Lowenstern, J.B., Mortensen, A., Pope, E.C., Bird, D.K., Reed, M.H., Friðleifsson, G.Ó., Elders, W.A., 2013. Composition and origin of rhyolite melt intersected by drilling in the Krafla geothermal field, Iceland. Contrib. Mineral. Petrol. 165, 327–347.